Laboratory acousto-mechanical study into moisture-induced changes of elastic properties in intact granite

Rui Wu[1], Paul Antony Selvadurai[1], Ying Li[1], Yongyang Sun[2], Kerry Leith[1], Simon Loew[1]

[1]Department of Earth Science, ETH Zürich, Zürich, Switzerland.
[2]Department of Exploration Geophysics, Curtin University, Perth, Australia.

Key Points:

- Laboratory time-lapse acousto-mechanical response of a freestanding intact granite specimen experiencing gradually wetting over 98 hours.
- Squirt flow dominates P-wave velocity increase in microcracked nanopore-dominated media.
- Changes in transmitted amplitude are explained and predicted by elastic wave propagation around P-wave first Fresnel zone.

Corresponding author: Rui Wu, `rui.wu@erdw.ethz.ch`

Abstract

The water adsorption into pore spaces in brittle rocks affects wave velocity and transmitted amplitude of elastic waves. Experimental and theoretical studies have been performed to characterize moisture-induced elastodynamic variations due to macroporous effects; however, little attention has been paid to the manner in which wetting of nanopores affect elastic wave transmission. In this work, we extend our understanding of moisture-induced elastic changes in a microcracked nanopore-dominated medium (80 % of the surface area exhibits pore diameters below 10 nm). We studied acousto-mechanical response resulting from a gradual wetting on a freestanding intact Herrnholz granite specimen over 98 hours using time-lapse ultrasonic and digital imaging techniques. Linkages between ultrasonic attributes and adsorption-induced stress/strain are established during the approach of wetting front. We found that Gassmann theory, previously validated in channel-like nanoporous media, breaks down in predicting P-wave velocity increase of microcracked nanopore-dominated media. However, squirt flow – a theory recognized to characterize wave velocity increase and attenuation in microcracked macropore-dominated media at pore scale – also accounts for the observed increase of P-wave velocity in microcracked nanopore-dominated media. The transmitted amplitude change in direct P waves are explained and predicted by the elastic wave propagation within P-wave first Fresnel zone and reflection/refraction on the wetting front.

Plain Language Summary

Rainfall, melting snow, dew, and fog that occurs at the earth's surface have all been shown to perturb elastic wave travel times, and decrease the amplitude of transmitted elastic waves in crustal rocks. This moisture-induced elastic variation is highlighted in the stability of engineering structures (e.g. bridges, dams), geo-energy extraction, and landslide behavior. The observed elastic variations have been studied, particularly in rocks with cracks, by analyzing the propagation perturbation of the transmitted elastic waves. However, very little is known about how elastic waves change with water imbibition in intact rocks. In this study, a noninvasive assessment technique named as ultrasonic monitoring is utilized to probe natural nanopore-dominated granite undergoing gradual wetting. We observed that a shorter P-wave travel time can be attributed to the pore fluid squirt from microcracks into relatively round pore spaces. Changes in the transmitted amplitude around the P-wave onset is mainly caused by incident P-wave reflection and conversion on the moving water

front. Ultrasonic results are corroborated by simultaneous monitoring of the mechanical deformation.

1 Introduction

In the earth's crust, fluids can alter the material properties from near-surface to subsurface in various ways. Natural (e.g. precipitation, dew, fog, melting snow) or anthropogenic hydraulic activities (e.g. water injection, hydrocarbon production) can increase the moisture content of porous medium driven by capillary pressure, gravity and injection pressure differences. During wetting, water molecules are initially adsorbed onto grain boundaries followed by capillary condensation; liquids gradually fill, and (almost) fully saturate the interconnected pore space (Gor & Neimark, 2010; Gor & Bernstein, 2016). This process induces changes in elastic properties; these have been reported in numerous *in situ* observations, varying from near-surface natural hazards, e.g. landslides related to groundwater movement or rainfall (Loew et al., 2017; Burjánek et al., 2017; Le Breton et al., 2021), engineering structure stability, e.g. thin sheet collapse of borehole/tunnelling wall (Diederichs, 2007), building material decay due to fluctuating humidity (McBain & Ferguson, 1927); and subsurface geo-energy applications involving with water flooding, e.g. oil and gas recovery, geothermal energy extraction (Landrø, 2001). Observed moisture-induced elastic variation almost always change the propagation of elastic waves in host materials. Characterization of moisture-induced variation of elastic properties, using the theory of elastic wave propagation, plays a central role in rock-physics research (Saito, 1981; Mavko et al., 2020).

1.1 Background on elastic response of porous media during water imbibition

The study of the dynamic elastic response of porous media to water imbibition has been reported from numerous laboratory and analytical studies performed on dry and saturated rocks over the past 70 years (Gassmann, 1951; Nur & Simmons, 1969; Winkler & Nur, 1979; Toksöz et al., 1979; Johnston et al., 1979; Mavko & Nur, 1979; Murphy III, 1982; Knight & Nolen-Hoeksema, 1990; Walsh, 1995; Gurevich et al., 2010; Mavko et al., 2020). High-frequency elastic waves (usually tens of kHz to MHz for laboratory measurements) are produced by ultrasonic piezoelectric transmitters and are then detected by ultrasonic receivers, which use the amplitude and wave velocity information to estimate their sensitivity to the presence of pore fluid. There is a large compendium of research on the underlying mechanisms of elastic changes due to moisture ingress into macroscopic pores; however, little attention has been paid to nanopores with pore widths below 100 nm defined by Thommes et al. (2015). This gap in the experimental understanding to explain the differences between wave propagation in macropore- and nanopore-dominated media lead to this study.

In laboratory ultrasonic tests, the P-wave velocity is widely observed to increase when macroporous, clay-deficient rocks become (almost) fully saturated with water. This P-wave velocity increase, under zero confining pressure, has been reported in sandstone as 8 to 73 % (King, 1966; Han, 1987; Coyner, 1984; Mavko & Jizba, 1991; Wang et al., 2021); granite as 8 to 27 % (Nur & Simmons, 1969; Saito, 1981; Coyner, 1984); limestone as 0 to 73 % (Nur & Simmons, 1969; Coyner, 1984; Agersborg et al., 2008) and dolomite as 28 % (Nur & Simmons, 1969). Various physical mechanisms have been proposed to predict such P-wave velocity increase; for example, Gassmann's equation (Gassmann, 1951), Biot's theory (Biot, 1956) and the squirt flow model (Mavko & Jizba, 1991; Gurevich et al., 2010). Extensive review of these models are given by Müller et al. (2010) and Mavko et al. (2020, Chapter 6).

Gor and Gurevich (2018) accurately modeled P-wave modulus changes in Vycor glass saturated by n-hexane (Page et al., 1995) and argon (Schappert & Pelster, 2013) within the framework of classical Gassmann theory (Gassmann, 1951; Berryman, 1999). Vycor glass in their study is a well-defined nanoporous medium characterized by channel-like pores with a peak throat size of around 7 to 8 nm (Levitz et al., 1991). However, when studying P-wave velocity increase in natural nanoporous media, such as rocks, the microstructural differences between e.g. man-made Vycor glass should not be ignored. Microcrack-based microstructures in rocks contribute to the bulk elastic changes more than round pores under varying confining pressure (Shapiro, 2003) or with the addition of pore fluid (O'Connell & Budiansky, 1977). It is premature to extend the validity of Gassmann theory to nanopores in microcracked media due to the added complexities of microcracks not present in the man-made Vycor glass (Gor & Gurevich, 2018; Dobrzanski et al., 2021). To the authors' knowledge, there are no classical theories (e.g. Gassmann theory) relevant to materials that contain both nanopores and microcracks. As almost all natural rocks contain a full range of pore sizes, understanding such material is fundamental to earth science research.

The amplitude decay of transmitted ultrasonic waves has been linked to the elastic properties of porous media (Johnston et al., 1979) and it is more sensitive than wave velocity to increases in the moisture content. Laboratory earlier studies of ultrasonic monitoring showed that observed losses in transmitted amplitude were an order of magnitude larger than variations in wave velocity when the dry specimen was saturated (Winkler & Nur, 1979, 1982). To study ultrasonic amplitude changes to the movement of wetting front, researchers (Wulff & Mjaaland, 2002; David, Sarout, et al., 2017; Pimienta et al., 2019; Thery et al., 2020) performed water imbibition tests by submerging part of the macroporous rock specimen into a water tank below. The wetting front was driven by capillary force, where free water first wets or saturates compliant microcracks at the grain scale. They pre-installed the transmitter-receiver pairs on the specimen surface and analyzed ultrasonic signature changes with the movement of the fluid front through time. They found a significant decrease in the transmitted wave amplitude even before the entire specimen was wetting. Moreover, this water imbibition process was found to be reversible by drying (Wulff & Mjaaland, 2002). Fluid (or solvation) pressure inside the pore spaces is generated (Gor & Neimark, 2010; Gor & Bernstein, 2016), which decreases the normal stress across microcracks (Li et al., 2021). This process also decreases contact stiffness around the grain contact (Yurikov et al., 2018) and friction coefficient along microcracks (Johnston et al., 1979). Passage of the elastic waves causes more relative mechanical deformation along/across microcracks and induce fluid flow within microcracks at the grain scale; as a result, more transmitted wave amplitude can be decayed (Mavko & Nur, 1979; Johnston et al., 1979; Walsh, 1995).

Ultrasonic-derived changes in elastic properties can be better understood if simultaneous low-frequency mechanical deformation data is available. Ultrasonic monitoring and mechanical deformation measurements have been jointly performed in macropore-dominated rocks, e.g. Bentheim sandstone (Yurikov et al., 2018) and Thringer sandstone (Tiennot & Fortin, 2020). Most of pore diameters were measured as 40 μm (Saenger et al., 2016) for Bentheim sandstone. Yurikov et al. (2018) quantified adsorption-induced deformation (extensional strain of the order of 10^{-4}) and elastic modulus reduction (e.g. a P-wave velocity decrease of 13 to 16 %) when the relative humidity (RH) was gradually increased from 13 to 97 %. They attributed that the observed elastic weakening/softening to be the result of solvation pressure generated in the pore space (2 to 3 MPa in Bentheim sandstone and 18 MPa in Thringer sandstone). Li et al. (2021) moved the focus from macropore- to nanopore-dominated rocks by studying Herrnholz granite, where the majority of pore diameters are below 10 nm. They gradually wet two free-standing 90 × 65 × 35 mm Herrnholz granite prisms using distilled water, which maintained water ingress from their upper surfaces.

Using digital image correlation (DIC) techniques, they found extensional strain with magnitudes up to 4.7×10^{-4} on the front face of prisms and calculated a solvation pressure of 40 to 47 MPa. This provided the initial mechanical constraints of the "hygroscopic expansion" process in this geomaterial.

1.2 Our study

There are no studies on the acousto-mechanical response to water imbibition in media containing nanopores and microcracks with the approach of a wetting front. It is not yet clear how P-wave velocity, transmitted amplitude and characteristic frequency respond as the water is imbibed into the nanopore space. Moreover, these changes in the ultrasonic features have not been compared with adsorption-induced deformation at relatively low frequencies. To this end, we conducted time-lapse ultrasonic pulse transmission in conjunction with DIC measurements in the Herrnholz granite subject to wetting. Waveform signature changes were analyzed: P-wave velocity and transmitted amplitude. We modeled the P-wave velocity changes with complementary hydrostatic compression tests. We also analyzed changes in ultrasonic wave amplitude in direct waves during the approach of a wetting front while simultaneously monitoring the adsorption-induced deformation throughout the entire experiment.

2 Material description

The Herrnholz granite used in these tests was obtained from the eastern side of a rock quarry located in Hauzenberg, Bavaria Germany. The rock contains nanopores and microcracks and exhibits a homogeneous fine-grained structure; it has been well characterized with respect to its petrophysical and geomechanical properties in recent studies (Li et al., 2021, 2022).

2.1 Thin section analysis

Petrographic thin section analysis of the intact specimen (35 mm $\times$ 22 mm $\times$ $30 \pm 5 \mu m$) revealed a granitic mineralogical assemblage of 50 % quartz, 38 % feldspar, and 11 % mica by area (Li et al., 2021). There were observed to be several types of feldspar (plagioclase, perthite and microcline) and mica (biotite, muscovite). We assumed properties of feldspar and mica can be represented by plagioclase and biotite, respectively. We adopted the elastic parameters of these minerals from Mavko et al. (2020, Table A.4.1) and estimated the effective elastic moduli from Voigt upper bound, Reuss lower bound and Hill average (Voigt, 1910; Reuss, 1929; Hill, 1952). The bulk (K_{gr}) and shear (G_{gr}) moduli from Hill average were 49.4 and 31.1 GPa, respectively. We provided the mineral moduli and effective elastic moduli of Herrnholz granite in Table S1 of the Supporting Information.

Crystal sizes of Herrnholz granite range from approximately 0.03 to 1 mm with an average size of 0.23 mm and a standard deviation of 0.13 mm. In the following sections, we targeted ultrasonic waves that exhibit a wavelength above around 5 mm at the frequency below 1 MHz. The minimum wavelength (5 mm) utilized in this study is one order of magnitude larger than the mean crystal size so that we assumed that the scattering effect on the ultrasonic wave attenuation would be negligible.

Thin sections were dyed with a fluorescent pigment and were observed under crossed-polarized and ultraviolet light. In Figure 1, we showed the microcrack geometry distribution. Within boxes colored by purple, black, cyan and yellow, four classes of microcracks were observed: cleavage cracks (nearly straight and parallel distribution inside a grain), grain boundary cracks, intergranular cracks (penetrating from grain boundaries to the grain inner) and intragranular cracks (random or parallel distribution inside a grain).

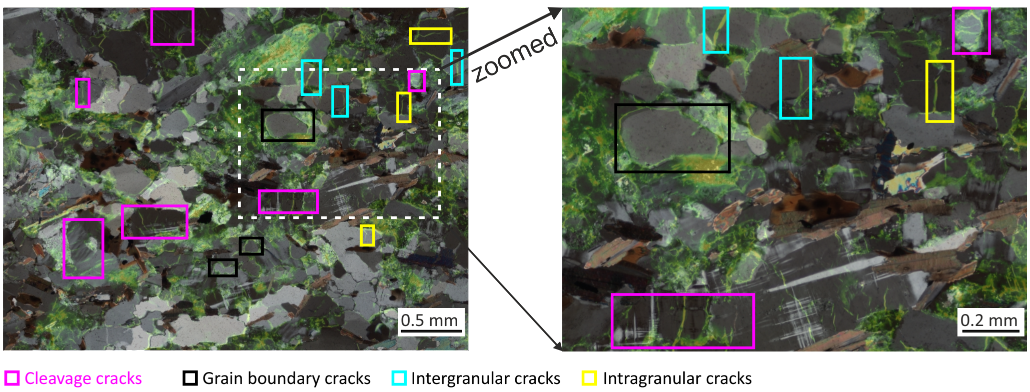

Figure 1. Superimposed micromosaic obtained with crossed-polarized light and ultraviolet light, indicating regions of cleavage cracks (purple box), grain boundary cracks (black box), intergranular cracks (cyan box) and intragranular cracks (yellow box) (Qtz: quartz; Kfl: K-feldspar; Prt: perthite; Bt: biotite; Mu:muscovite) (reproduced with permission from Li et al. (2021) (CC BY-NC-ND 4.0))

2.2 Density, porosity and pore size distribution

Density, porosity and pore size distribution were quantified using a combination of *1*) gas pycnometry, *2*) mercury intrusion, *3*) nitrogen adsorption, and *4*) water saturation methods at ClayLab and Rock Physics and Mechanics Laboratory at ETH Zurich.

We measured the grain density (ρ_{gr}) over two prismoid specimens (dimension: 25 mm $\times$ 25 mm $\times$ 40 mm). These specimens were oven-dried at a temperature of 80 $°C$ for at least 72 hours. During the drying process, specimens were weighed every 24 hours until variations in weight were below 0.01 %. We used a helium pycnometer (model: AccuPyc II 1340) to measure their matrix volume as 22.7228 $\pm$ 0.0118 cm^3 and 22.7834 $\pm$ 0.0235 cm^3, respectively. Specimens were weighed as 60.526 g and 60.681 g at a precision of 0.001 g, respectively. Grain density was derived as 2.664 $\pm$ 0.0014 g/cm^3 and 2.663 $\pm$ 0.0027 g/cm^3. We used 2.66 g/cm^3 as the average grain density.

To acquire the bulk density (ρ_b), three granite cylinders (100 mm in length, 50 mm in diameter) were oven-dried at 80 $°C$ following the same procedures in measuring the grain density. Bulk density was measured as the ratio of weight to volume, 2.609 g/cm^3 with an estimated uncertainty of 0.04 % (or 0.001 g/cm^3). The density difference between the grain and bulk density provided us a rough estimation of total porosity (ϕ_t) of 1.9 % $\pm$ 0.2 % over the granite cylinders.

To have access to the water-accessible porosity (ϕ_w), oven-dried granite cylinders were saturated by a de-airing technique (Selvadurai et al., 2011) lasting for 10 days. During the saturation process, specimens were kept in a vacuum chamber filled with distilled water at a vacuum pressure of 80 kPa to expel air. The specimens were weighed every 24 hours by first removing the surface water using a dry cloth. The saturation process was deemed complete when a weight change below 0.01 % was recorded. Water-accessible porosity was calculated to range between 1.45 % and 1.53 %. Estimated uncertainty was around 0.007 % in the total volume of the cylinder specimen. Detailed uncertainty analysis in measuring volume, density and porosity were provided in Section 1 of the Supporting Information.

Seven specimens (20 mm $\times$ 6.5 mm $\times$ 6.5 mm) were prepared to measure the mercury-accessible porosity (ϕ_{Hg}) through mercury intrusion at an intrusive pressure up to 400 MPa. Mercury-accessible porosity ranged from 0.72 % to 1.69 % with a mean porosity of around 1.15 %. The uncertainty in the mercury-accessible porosity was between 0.003 % to 0.005

% in the total volume of the prismoid specimen for individual measurements. Although Washburn's equation holds for the penetration of mercury through pore throats greater than around 3 nm (Washburn, 1921; Njiekak et al., 2018), intruded mercury volume maintained when the pore diameter was lower than around 10 nm. These pores and poorly connected pores were not open to mercury even up to 400 MPa. These pore volumes were not counted into the mercury-accessible porosity (conservative estimation of the realistic pore volumes), and were assumed to contribute to the difference among the total, water-accessible and mercury-accessible porosity.

To quantify the pore size distribution below 10 nm, Li et al. (2022, submitted to JGRSE) conducted the porosimetry of nitrogen adsorption over two specimens (40 mm $\times$ 10.5 mm $\times$ 10.5 mm) and revealed that around 80 % of the surface area of this granite exhibited pore diameter below 10 nm. More discussion on porosimetry results (Figure S1 and S2) and uncertainty analysis through mercury intrusion and nitrogen adsorption were provided in Section 2 of the Supporting Information.

2.3 Ambient P-wave velocity measurement

A suite of characterization tests were performed to quantify the P-wave velocity structure of our Herrnholz granite. We performed 3D ultrasonic tomography (Martiartu & Böhm, 2017) on three cuboidal specimens of granite with a side length of 160 mm under ambient conditions. Detailed experimental setup, measurement methodology and visualization of the P-wave velocity structure are provided in Section 3 of the Supporting Information. P-wave velocity structure and the P-wave velocity in each orthogonal direction were experimentally characterized and uniform, with 3981 ($\pm$ 69), 3977 ($\pm$ 60), and 3988 ($\pm$ 64) m/s. The estimated uncertainty was 1.72 %, 1.53 % and 1.60 %, respectively. To avoid specimen variability, we repeated the tests on other 2 specimens and found P-wave velocity of 3914 ($\pm$ 74), 3925 ($\pm$ 71), and 3982 ($\pm$ 64) m/s, respectively, with estimated uncertainty of 1.9 %, 1.8 % and 1.6 %, respectively. We assumed the density was homogeneous throughout the specimens. We concluded that there was very weak anisotropy, heterogeneity and specimen variability in the elastic moduli of Herrnholz granite.

2.4 Wave velocity measurement in hydrostatic compression test

We analyzed the stress dependence of the dynamic elasticity of Herrnholz granite from separate hydrostatic compression tests. Two granite, and an aluminum (model: EN AW-6082, for reference) specimens were tested under stepwise-increasing axial and confining pressure from 5 to 160 MPa. Granite specimens were prepared following the oven-dried (80 $^{\circ}C$) and saturation procedures described in Section 2.2. The detailed experimental facilities and design (e.g. loading rate) were detailed in Section 4 of the supporting information. P- and S-wave data were acquired and digitized at a sampling rate of 50 MHz. Waveforms were stacked 4000 times for one survey; once counting 60 surveys, we stored one survey into the connected DAQ system. Their onsets of first arrival were picked using the Aikake information criterion (AIC) technique (Akaike, 1974). Ultrasonic waveforms were shown between 15 to 40 μs in Figure 2. Triggering time was denoted by 0 μs. Note that the ultrasonic duration was corrected from the transmit time delay for P- (8.52 μs) and S-wave (13.32 μs) transmitter-receiver pairs (resonant frequency around 1 MHz) provided by the manufacturer of the ultrasonic test system (Wille Geotechnik).

When confining pressure was increased from 5 to 160 MPa (color evolved from dark to pink), P-wave first arrival in the dry specimen (22.42 to 17.46 μs) decreased much faster than the saturated case (18.86 to 17.22 μs). We showed S waveforms measured in the dry specimen and observed higher noise before S-wave first arrival. This was because of the weak response of S-wave transducer to the incoming P waves. We also attempted to measure S waveforms in the saturated specimen. However, we found their amplitude was strongly attenuated and almost merged into the background noise compared to the dry specimen. Meanwhile, S-wave first motion was relatively small and usually followed by a reflection of P-wave first motion from the back of the aluminium backing piece assembled with ultrasonic transducers. We failed to pick S-wave first arrival properly. Moreover, in this study, we focused on the P-wave velocity and amplitude changes. Therefore, we did not have the S-wave velocity analysis in the saturated specimen.

The P- and S-wave velocities of the oven-dried granite specimen (red circles) increased nonlinearly with the confining pressure P_c (5 to 160 MPa) from 4450 to 5731 m/s ($\Delta V_p =$ 1281 m/s) and 2736 to 3311 m/s (ΔV_s = 575 m/s), as shown in Figure 3(a) and (b), respectively. We estimated the uncertainties in wave velocity as around 0.32 % (or 18 m/s) for P waves and 0.31 % (or 10 m/s) for S waves, respectively. Detailed calculation process

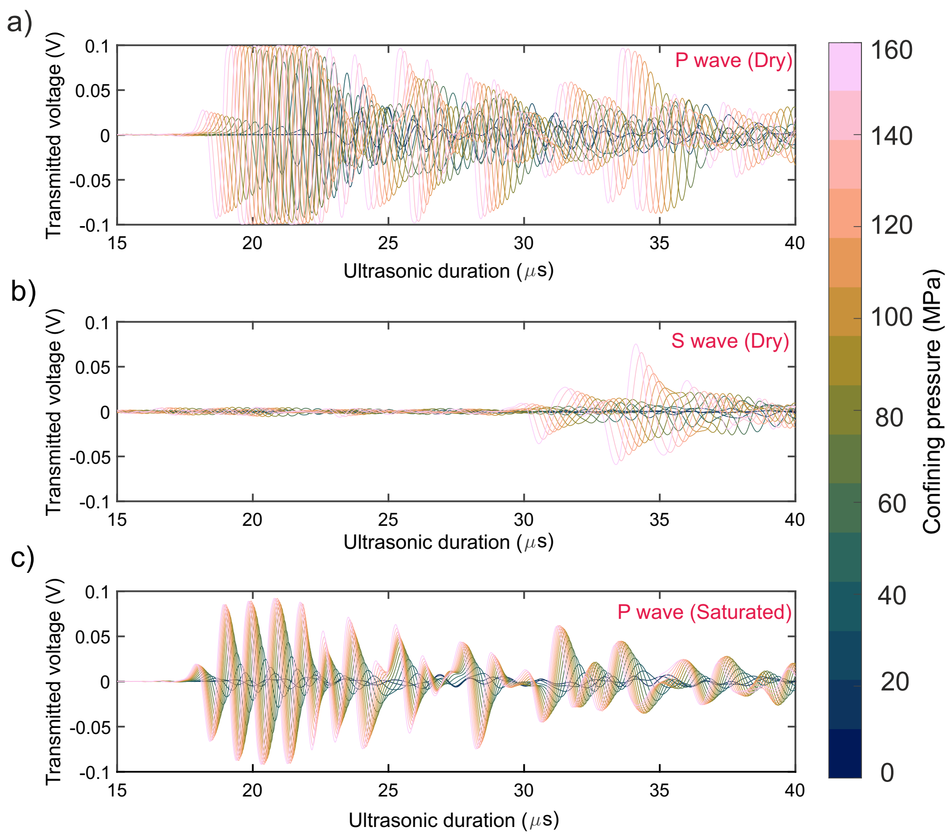

Figure 2. Ultrasonic waveforms measured in hydrostatic compression tests over (a) dry specimen using P-wave transmitter-receiver pair; (b) dry specimen using S-wave transmitter-receiver pair; (c) saturated specimen using P-wave transmitter-receiver pair.

was provided in Section 5) of Supporting Information. Overlapped symbols denoted values from repeated pulsing tests (about 50) at each confining pressure. These gave an estimated uncertainty based on the standard deviation among repeated tests (Christeson et al., 2018) and were around 12 m/s (P wave and dry), 8 m/s (S wave and dry), 2 m/s (P wave and aluminum), 15 m/s (P wave and saturated), and 1 m/s (S wave and aluminum) . The P-wave velocity in the saturated granite specimen (blue squares) increased from 5271 to 5804 m/s ($\Delta V_p = 533$ m/s). Almost constant P- ($\Delta V_p = 60$ m/s) and slowly increasing S-wave ($\Delta V_s = 103$ m/s) velocities were found in the reference test of aluminum specimen (grey crosses). Little velocity changes in aluminum could be possibly attributed to the loading system and, especially, the improved contacts between the ultrasonic transmitter-receiver pairs and the specimen (Pyrak-Nolte et al., 1990). No clear stress dependence of the elastic wave velocity was observed in the aluminum specimen.

2.5 Elastic piezosensitivity

We calculated the dynamic bulk (K_{dry}) and shear (G_{dry}) moduli using the expression $K_{dry} = \rho_b(V_p^2 - \frac{4}{3}V_s^2)$ and $G_{dry} = \rho_b V_s^2$ where V_p and V_s were P- and S-wave velocities of dry specimen, respectively (data from Figure 3(a) and (b)). Bulk density (ρ_b) of dry specimen was assumed as constant and given as 2.609 g/cm^3 from previous measurements in Section 2.2. When the confining pressure increased from 5 to 160 MPa, K_{dry} and G_{dry} ranged from 26.0 to 48.2 GPa and 19.8 to 28.9 GPa, respectively (red circles in Figure 3(c) and (d)).

We adopted a model of elastic piezosensitivity by Shapiro (2003) to evaluate the effect of microcracks (porosity and aspect ratio) on observed increase in the stress-dependent elastic properties. The model assumes a distribution of randomly oriented, isolated, penny-shaped microcracks in isotropic, linear, elastic medium (O'Connell & Budiansky, 1974). After reaching a confining pressure of 160 MPa, the specimen was unloaded at a stepwise-decreasing axial and confining pressure from 160 to 0 MPa. We provided the P- and S-wave velocities measured during the unloading stage in Figure S4 of the Supporting Information. We found that both P- and S-wave velocities recovered to within 70 m/s and 5 m/s, respectively, of their original values. This justified our assumption of elastic conditions required in the elastic piezosensitivitive model.

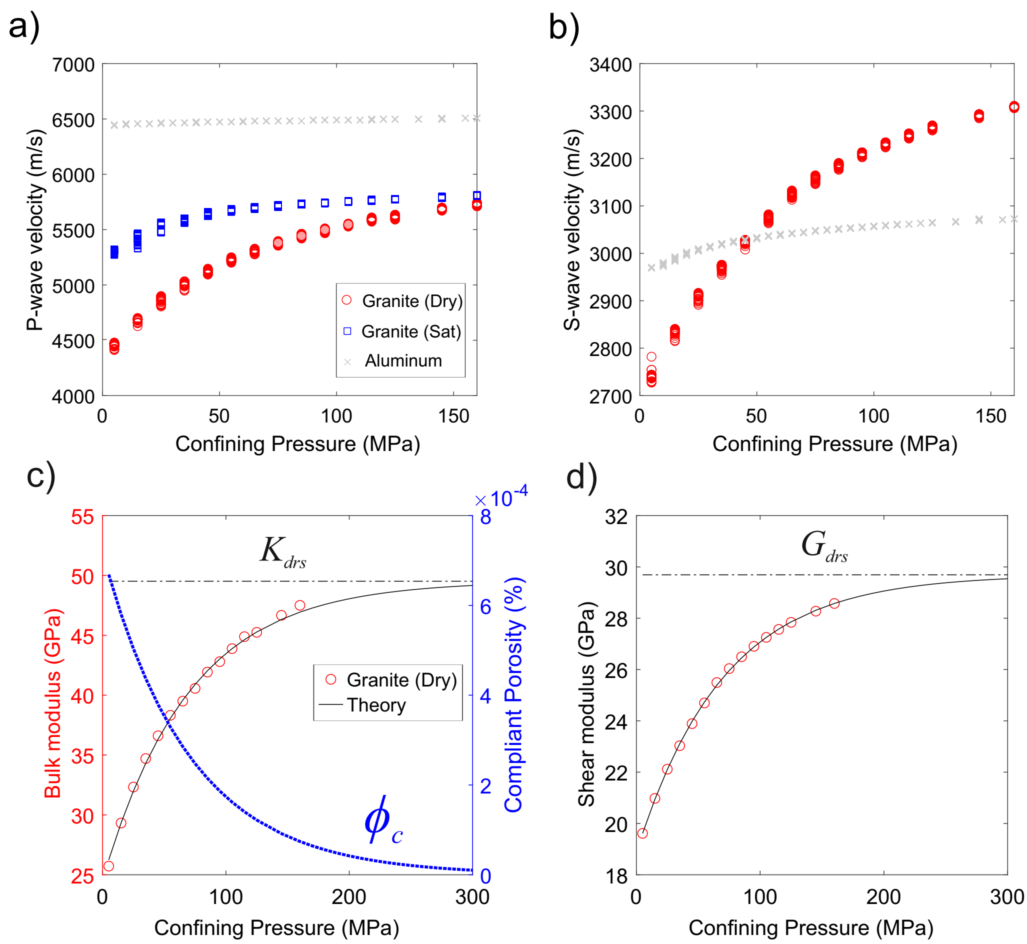

Figure 3. Wave velocities and elastic moduli from hydrostatic compression tests. (a) P- and (b) S-wave velocity changes in Herrnholz granite (red circles) and aluminum specimen (grey crosses) in response to a series of confining pressures (5 to 160 MPa). (c) Bulk and (d) shear moduli versus confining pressure (red circles: testing data; black lines: theory). Blue dashed line represents the compliant porosity evolution.

The elastic piezosensitivitive model offers a phenomenological explanation for the observed dependency of wave velocity with confining pressure. This model assumes that increases of wave velocity are only attributed to pore and crack closure and does not consider potential stiffening of the minerals that has been observed in other hydrostatic compression tests (Adams & Williamson, 1923; Brace, 1965; Wepfer & Christensen, 1991). Other models exist that estimate the crack porosity using stress dependence of elastic properties (Walsh, 1965; Cheng & Toksöz, 1979; Kuster & Toksöz, 1974; Berryman, 1980; Norris, 1985); however, the optimal selection of these models is outside the scope of this work and will be considered in the future.

Detailed mathematical description and parameter calculation of the Shapiro's piezosensitivity model were given in Section 6 of the Supporting Information. According to the theoretical description of K_{dry} and G_{dry} given in Equation S8 from the Supporting Information, we estimated the model parameters by minimizing the residual between the theories and experimental results iteratively. For penny-shaped microcracks, porosity $\phi_{c0} = 7.2 \times 10^{-4}$ without confinement and representative (average) aspect ratio $\alpha = 1.1 \times 10^{-3}$ were derived. The bulk (K_{drs}) and shear (G_{drs}) moduli of the hypothetical granite with a closed compliant porosity were calculated as 49.5 and 29.7 GPa, respectively. Note the difference between K_{gr} and K_{drs} (or G_{gr} and G_{drs}). K_{gr} and G_{gr} are the bulk and shear moduli of mineral grain and calculated from Hill average (see Table S1 in the Supporting Information).

In Figure 3(c) and (d), K_{dry} and G_{dry} (black solid line) derived from theory matched well the measured data (red circles) until 160 MPa. Above 160 MPa, theoretical solutions, extrapolated until 300 MPa, gradually approached constant values (black dashed line) which were given by K_{drs} and G_{drs}. Compliant porosity ϕ_c (blue dashed line) decreased by two orders of magnitude: 7.2×10^{-4} at 0 MPa to 1×10^{-5} at 300 MPa, which was almost completely closed. These piezosensitive parameters will be used in the modeling of P-wave velocity increase later.

3 Free-standing wetting test

The aim of the main experiment reported in this study is to understand the acousto-mechanical response in nanopore-dominated geomaterial that experience hygroscopic expansion in response to gradual wetting. To quantify this effect, we build on the time-lapse monitoring methods of ultrasonic (Schmitt et al., 2005; Njiekak et al., 2013; Yurikov et al., 2018) and digital image correlation (DIC) (Li et al., 2021) methods in the Herrnholz granite.

3.1 General setup

Water imbibition tests were performed on an intact, free-standing "prismoid" specimen of Herrnholz granite (dimension: $65 \times 35 \times 90$ mm) as shown in Figure 4(a). The specimen was initially oven-dried at a temperature of 80 $°C$ for at least 72 hours; meanwhile, it was weighed every 24 hours until variations in weight were below 0.01 %. Then the specimen was allowed to naturally acclimate to ambient conditions for 18 hours. Water was introduced to the specimen via a filter paper that was immersed in a water reservoir ($\sim$15 mm above the specimen). Aluminium blocks kept the filter paper in contact with the top of the specimen and water was drawn onto the top surface by capillary forces. Distilled water was used to fill and replenish the reservoir (0, 26, 47, 71 hours) over 80 hours. This ensured an almost constant infiltration and imbibition of fluids into the top half of the sample that contained the region of interest (ROI) for the DIC measurements.

3.2 Time-lapse DIC observation

A time-lapse DIC technique was utilized to measure the moisture-induced deformation on the front face of the granite specimen. In Figure 4(a), a schematic depiction of the digital camera (model: Sony Alpha A7RII with 43.6 total megapixels) was shown; this was mounted and locked to position 240 mm from the surface of the specimen. We used the natural fine-grained granite texture as the speckle pattern, and the front surface of the specimen was imaged at 2-minute interval and 1/13-second exposure time. A low-power Sony LED macro flash was triggered by the camera shutter in order to create consistent lighting for the images without affecting the specimen temperature.

Prior to introducing water, the specimen was allowed to equilibrate for 18 hours at ambient conditions. This allowed us to evaluate the displacement and strain baselines in the absence of water. The region of interest (ROI), as shown as the pink patch in Figure 4(b), was located 3 to 4 mm from the top and side edges to minimize boundary effect, with 58 mm in width and 40 mm in height (symmetrical about the y position of the transmitter-receiver pair). We used the open source Ncorr software (Blaber et al., 2015) to calculate the surface deformation from captured images over 98 hours. This method tracks surface

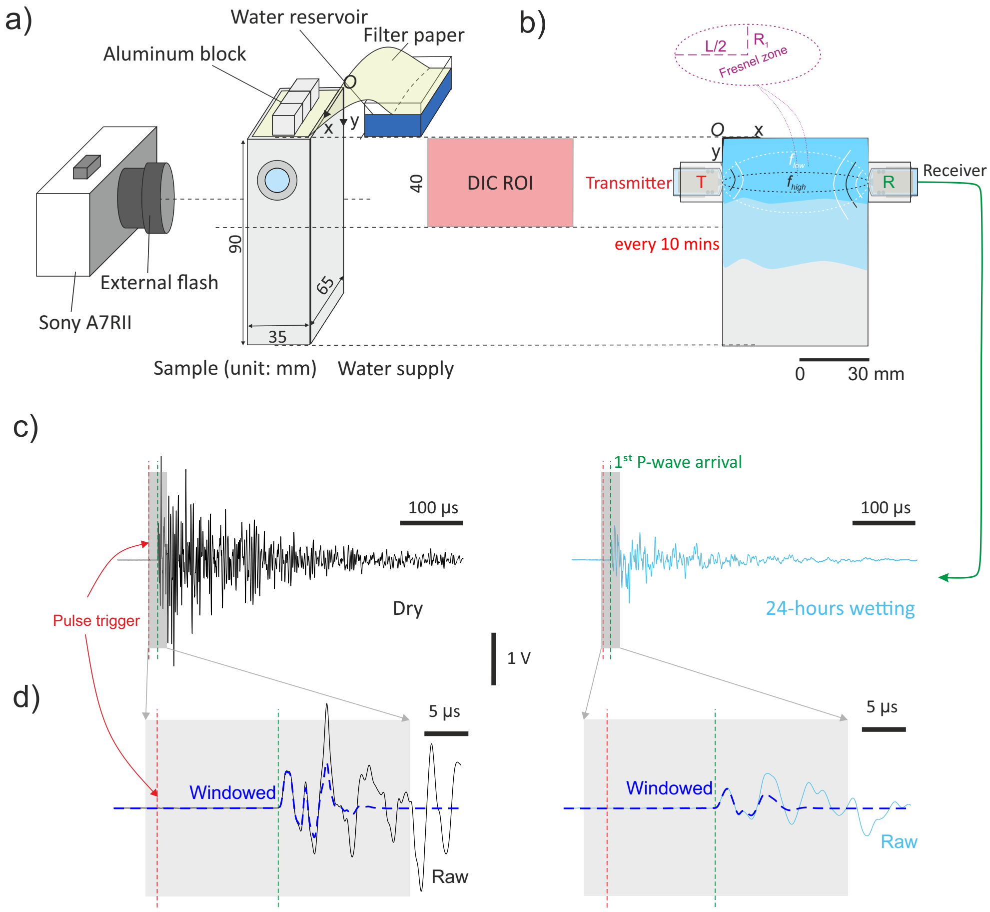

Figure 4. Schematic diagram of the experimental setup. (a) A free-standing granite prism (90 65 35 mm) of which upper part was subjected to gradual wetting. Mechanical moisture-induced deformation was measured on the vertical front surface in the region of interest (ROI) using digital image correlation (DIC). Figure (a) was adapted with with permission from (Li et al., 2021). (b) Ultrasonic pulsing was performed using a PZT transmitter coupled to the vertical surface 20 mm from the top of the sample. (c) Raw transmitted waveforms: dry (black) and wet (blue) measurements. (d) Windowed transmitted waveforms centered around the first P-wave arrival used for the spectral analysis.

deformation by correlating the best fit between pixel values within a defined search window, named subset, in a current image to those in the reference image. We set the subset radius as 50 pixel or 0.8 mm (equivalent to several crystals given the mean grain size of 0.23 mm), which on one side reduced the noise, and from the other side allowed us to track deformation at a resolution similar to the grain size. To calculate strain from the displacement field, a strain-window radius of 15 pixel (equivalent to 0.24 mm) was set.

3.3 Time-lapse ultrasonic monitoring

We adopted pulse transmission technique (Birch, 1960; ASTM D-18, 2008; Aydin, 2015) to study changes of ultrasonic waveform in response to water imbibition through time. In Figure 4(b), we showed the PCT-MCX transmitter (left, red T) and the KRNBB-PC receiver (right, green R) that were installed using aluminum cylinder holders at the height of $y = 20$ mm. The PCT-MCX transmitter was custom-built and its design and source characteristics were well documented in Selvadurai et al. (2022). The KRNBB-PC receiver was provided by KRN Services and was absolutely calibrated in Wu et al. (2021) – flat instrumental response between 100 kHz to 1 MHz. Later spectral analysis is performed over this frequency bandwidth. Both transmitter and receiver followed the design of point-contact transducers to eliminate the sensor aperture effect (Eitzen & Wadley, 1984; Glaser et al., 1998). These point-contact sensors have a tip aperture diameter of 1.5 mm.

The aluminum holders were coupled directly to the sample surface using cyanoacrylate and were threaded; this allowed the ultrasonic transducers to press against the surface of the specimen with their threaded casing. For this test, a high-voltage impulse source of 500 V was applied to the PCT-MCX transmitter using the same pulsing system described in Section 3 of Supporting Information. Pulses were emitted every 10 minutes over $\sim$ 98 hours. Recordings were taken around the trigger (before: 50 μs, after: 500 μs) to capture the wave information. Due to the more rapid transient response of the rock during the initial portions of the wetting, pulsing was performed every 2 minutes for 2 hours after wetting commenced. Waveforms of the receiver were recorded at 20 MHz. The same DAQ system were used as in Section 2.3.

We used the Aikake information criterion (AIC) (Akaike, 1974) to pick the onset of the P-wave arrival starting from the triggering time until 35 μs. Triggering time was denoted by 0 μs. This technique has been effective in laboratory ultrasonic studies (Kurz et al., 2005).

We provided one example in Figure S5 of the Supporting Information. We picked the onset of P-wave first arrival at the location of minimum AIC value. We calculated the P-wave velocity using the ratio between specimen width ($L = 65$ mm) to the duration between the triggering time and P-wave first arrival.

3.4 Frequency-based volume of the Fresnel zone

The transmitter-receiver arrangement generated a Fresnel zone, defined as a confocal prolate ellipsoidal region between transmitter and receiver (Spetzler & Snieder, 2004). A schematic representation was shown in Figure 4(b) but the size of the Fresnel zone was dependent on the specimen width and the frequency bandwidth of interest. Since the Fresnel zone had an ellipsoidal geometry, we used the same nomenclature as an ellipse to describe the Fresnel zone. The elastic properties of this zone were mostly revealed by band-limited direct waves propagating along the transmitter-receiver straight ray path. The boundary of the Fresnel zone consisted of points at which the difference in the propagation distance between direct-path and deflected-path waves on the boundary was a multiple (n) of the half wavelength, $\lambda/2$. In this study, we focused on the P-wave first ($n = 1$) Fresnel zone (P-FFZ), which gave the radius R_1 of the ellipsoid minor axis as:

$$R_1 = \frac{1}{2}\sqrt{\lambda L + \frac{\lambda^2}{4}}. \tag{1}$$

Equation 1 is only valid for a homogeneous medium. In our experiment it provided a rough estimate of R_1 when the wetting front moved towards the bottom surface, with introduced heterogeneity around the transmitter-receiver straight ray path.

3.5 Data reduction techniques

Examples of waveforms measured under the dry (black) and wet (blue) stages showed significantly attenuated elastic waves due to water ingress in Figure 4(c). Pulse trigger time and first P-wave arrival were denoted by red and green lines, respectively. To avoid spectral leakage and focus the analysis on the direct P-wave phase that mostly exhibits elastic changes inside P-FFZ, the waveforms were windowed using a Blackmann-Harris window centered about the onset of first P-wave arrival. We showed details in direct waves within the grey box in Figure 4(d). Windowed and raw waveforms were denoted by dashed and solid line, respectively. The window duration (e.g. grey box width) of 30 μs (roughly twice the travel time from transmitter to receiver) was set to ensure that it would contain essential information on the direct P-wave phases and also at a satisfactory resolution $\sim$ 100 kHz, which was defined by Wu et al. (2021).

To quantify the attenuation effect, the fast Fourier transform (Bracewell, 1986) was performed to study the spectral content of transmitted amplitude from 100 kHz to 1 MHz. We calculated transmitted amplitudes as well as the noise level of waveforms shown in Figure 4(d) and presented them in the frequency domain in Figure S6 in the Supporting Information. We found there was sufficient transmitted amplitude until 1 MHz comparing to the noise level under dry conditions; however, transmitted amplitude close to 1 MHz under wet conditions could be not easily differentiated from the noise level. This is another reason we chose 1 MHz as the upper limit of frequency bandwidth.

We observed that waveforms acquired at sufficient wetting could merge into the noise level without signal amplification. We connected the receiver with a pre-amplifier system (Elsys AE-AMP) that allowed us to select gain settings of 0 dB, 20 dB, or 40 dB. This pre-amplifier could filter the acquired signal with a passband frequency range so that the background noise could be effectively depressed while the signal was amplified (Bertschi, 2018). We adopted 40 dB gain to ensure extraction of the necessary message throughout the entire wetting stage.

4 Results

4.1 Moisture-induced changes in ultrasonic signatures

We analyzed the changes in transmitted direct waves over 98 hours (18 hours under ambient conditions and 80 hours of wetting). In Figure 5(a), we showed the stacked and aligned raw waveforms of 630 surveys and a visualization of the direct wave phases from -2 to 30 μs. Ultrasonic duration was the duration offset from the pulse triggering time. An ultrasonic duration equal to 0 μs referred to the triggering time of pulsing tests (green dashed line). A wetting time equal to 0 hour denoted the time that distilled water arrived on the top surface of the specimen through the filter paper. Image color represented the magnitude of transmitted voltage ranging from -2 to 2.6 V (red: positive, blue: negative and white: 0 value).

Transmitted amplitude was shown between the bandwidth of 100 kHz to 2 MHz in the frequency domain (Figure 5(b)). We converted the waveform amplitude (unit: V) into amplitude (unit: dB) using $A(\text{dB}) = 20 \times \log_{10}(A(\text{V}))$. The image color indicated the magnitude of the transmitted amplitude, ranging from -45 to -8 dB (changes in the order of magnitude of 2).

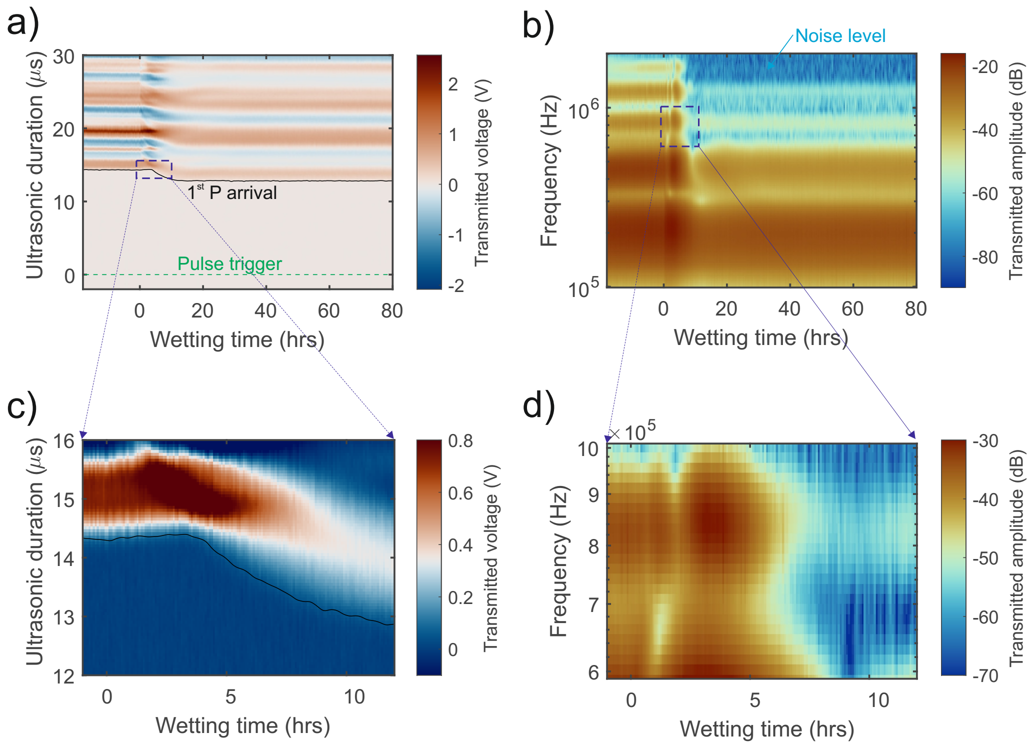

Figure 5. Changes in stacked ultrasonic waveforms over 98 hours in response to water availability. Direct waves in (a) time domain (duration: -2 to 30 μs) and (b) frequency domain (frequency bandwidth: 100 kHz to 2 MHz). For details around the P-wave first arrival, direct waves were isolated between -1 to 12 hours in (c) time domain (duration: 12 to 16 μs) and (d) frequency domain (frequency bandwidth: 600 kHz to 1 MHz). The onset of the P-wave first arrival was shown in black and was illustrated more prominently in Figure 6.

4.1.1 Changes in P-wave arrivals

We were interested in the changes in P-wave first arrivals upon the introduction of water and thus we isolated the results within a purple box within a wetting time of -1 to 12 hours and an ultrasonic duration of 12 to 16 μs in Figure 5(a) to Figure 5(c). We found the onset of P waves (black line), calculated using AIC technique (Akaike, 1974), progressively decreased from 14.4 to 12.8 μs at an uncertainty of 50 ns between 0 to $\sim$ 16 hours. Uncertainty of P-wave velocity was around 0.25 % (or 13 m/s) estimated in Section

5 of the Supporting Information. In Figure 6(a), P-wave velocity was initially measured at approximately 4538 m/s over 18 hours, decreased very slightly to 4507 m/s from 0 to 3.2 hours, and rose to a plateau (5074 m/s) at approximately 16 hours. The onset of S waves was not included in this study because multiple reflections from the outer boundaries between the P- and S-wave onset masked the first arrival of the S waves.

4.1.2 Changes in transmitted amplitude of direct waves

In Figure 5(c), we showed the transmitted voltage between -0.1 to 0.8 V using a narrow color scale to highlight the amplitude changes around the P-wave arrival. We found the P-wave first peak was amplified (red to deep red) after the introduction of water and later attenuated (deep red towards white) to lower value. We picked the location of first peaks and showed their amplitudes in Figure 6(b). The amplitude maintained stable (0.71 ± 0.015 V) before 0 hour, increased to 1.07 ± 0.01 V around 3.2 hours, decreased to 0.33 ± 0.01 V around 11 hours followed by little recovery below 0.06 V. The amplitude maintained at 0.38 V $\pm$ 0.007 V after 16 hours.

We found that changes in the transmitted amplitude upon wetting was frequency-dependent. For example, in Figure 5(b), there was a significant amplitude decrease (above 15 dB) above around 600 kHz and less amplitude decrease (below 5 dB) below around 300 kHz. Due to our understanding of the ultrasonic transducers, it is feasible to analyze the bandwidths over low frequency (LF = 100 to 300 kHz), middle frequency (MF = 300 to 600 kHz), and high frequency (HF = 600 to 1000 kHz). We isolated the results within a purple box within a wetting time of -1 to 12 hours and frequency of 600 to 1000 kHz in Figure 5(b) to Figure 5(d). We monitored the transmitted amplitude and found it to decreased after 3 to 4 hours of wetting.

We calculated the mean changes in the transmitted amplitude in dB and showed them at three frequency bandwidths (LF, dashed line; MF, dotted line; and HF, solid line) in Figure 6(c). We introduced six times from O to v that were turning points of P-wave velocity as well as the transmitted amplitude changes at HF. Time O (0 hour) was marked as the thick blue line in Figure 6. The subsequent times i (1.3 hours), ii (3.2 hours), iii (9 hours), iv (16 hours) and v (32 hours) were shown as blue dashed vertical lines. Changes in the transmitted amplitude in direct waves were denoted as ΔT_d.

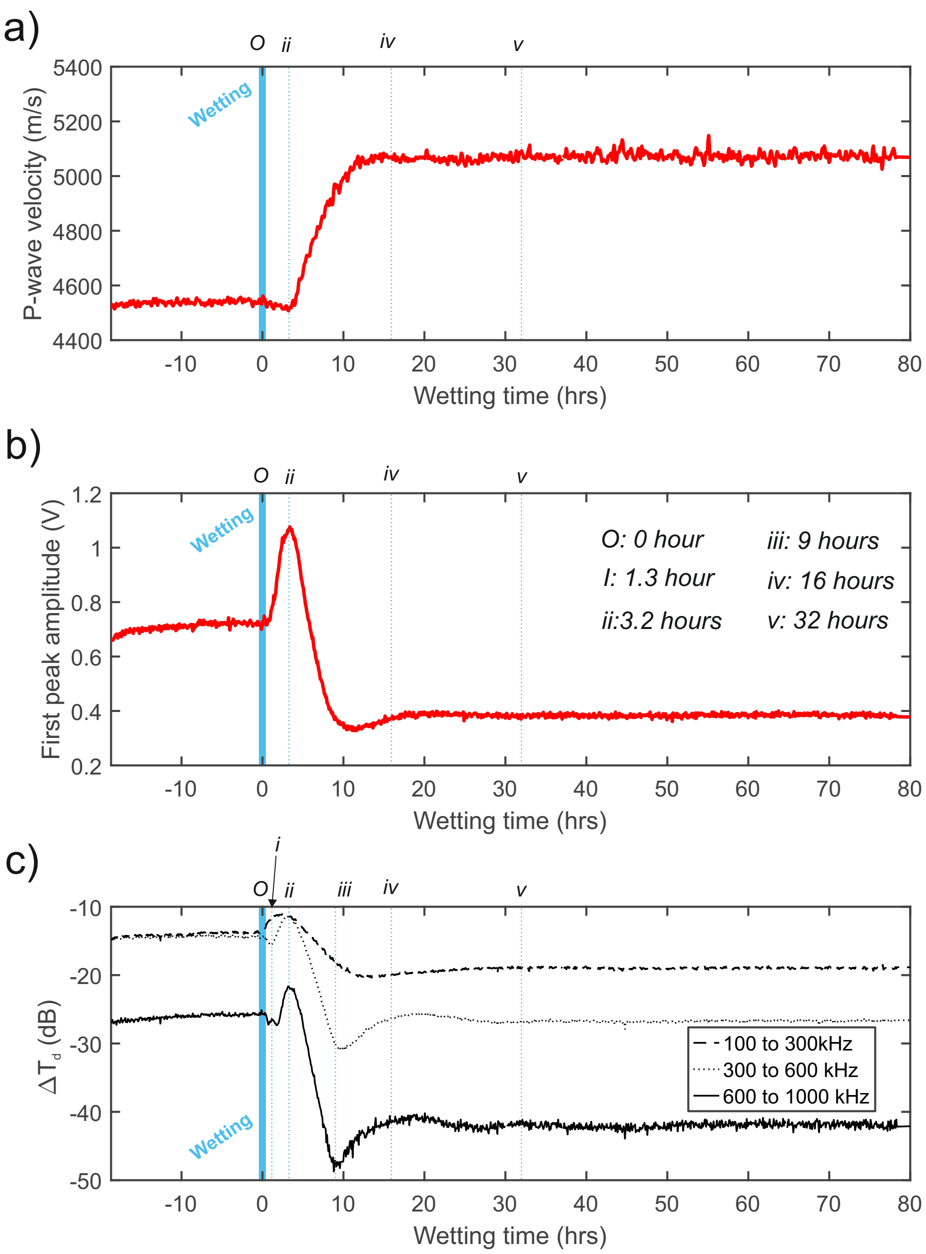

Figure 6. Changes in ultrasonic signatures over 98 hours in response to water availability. (a) Measured P-wave velocity between 4538 and 5074 m/s. Transmitted amplitude averaged at three frequency bandwidths (100 to 300 kHz, 300 to 600 kHz, and 600 to 1000 kHz) for direct waves. These frequency bandwidths were denoted as *LF*-low frequency, *MF*-medium frequency, and *HF*-high frequency, respectively. Vertical blue dashed lines indicated a few turning point of transmitted amplitude and P-wave velocity.

Prior to time O, specimen remained in a steady state since transmitted amplitudes in direct waves were stable (all variations below 1 dB). Once water was introduced to the top surface of the specimen (time O at 0 hour), ΔT_d increased from time i to ii (1.3 to 3.2 hours) as the frequency bandwidth changes (ΔT_d^{LF} = + 2.6 dB, ΔT_d^{MF} = + 3 dB and ΔT_d^{HF} = + 4 dB). As the time increased, i.e., ii to iii (3.2 to 9 hours), ΔT_d began to decrease as the bandwidths were changed (ΔT_d^{LF} = − 9.0 dB, ΔT_d^{MF} = − 19.5 dB and ΔT_d^{HF} = − 27 dB). After time iii (9 hours), ΔT_d started to recover at all bandwidths (ΔT_d^{LF} = + 0.6 dB, ΔT_d^{MF} = + 5.5 dB and ΔT_d^{HF} = + 8 dB) and stabilized at time iv (18 hours) with a ± 0.1 dB change over all bandwidths.

Throughout the wetting stage (0 to 80 hours), the total ΔT_d at different frequencies was − 4.6 dB (LF), − 12.6 dB (MF), − 17 dB (HF), respectively.

4.1.3 P-wave quality factor measurement

Spectral ratio method (Toksöz et al., 1979) was utilized in this study to characterize seismic wave attenuation of Herrnholz granite independent of frequency under dry and wetting conditions. Ultrasonic monitoring of pulse transmission was performed using the same procedures that were used in the wetting experiment on Herrnholz granite specimens and a reference material, aluminum. The aluminum (model: EN AW-6060) was used due to its extremely low attenuation with respect to rocks (Zemanek & Rudnick, 1961). The geometry of the aluminum specimen was identical to the Herrnholz granite specimen shown in Figure 4. The amplitude (A) of plane elastic body waves at the specific frequency for the aluminum (subscript 1) and Herrnholz (subscript 2) specimens can be expressed as:

$$A_1(f) = G_1(x)e^{-\frac{\pi f x}{Q_1 v_1}} e^{i(2\pi f t - k_1 x)}, \tag{2a}$$

$$A_2(f) = G_2(x)e^{-\frac{\pi f x}{Q_2 v_2}} e^{i(2\pi f t - k_2 x)}, \tag{2b}$$

where f and k are the frequency and wavenumber of the received waveforms, v is the P-wave velocity, x is the distance between transmitter and receiver (65 mm) and $G(x)$ is a frequency-independent geometrical factor that includes geometrical spreading and reflections.

Windowed waveforms of direct waves were shown in time (Figure 7(a)) and frequency domain (Figure 7(b)). Waveforms measured in the Herrnholz granite were aligned at the P-wave first arrival. Before the wetting stage (below 0 hour), waveforms (grey line) overlapped

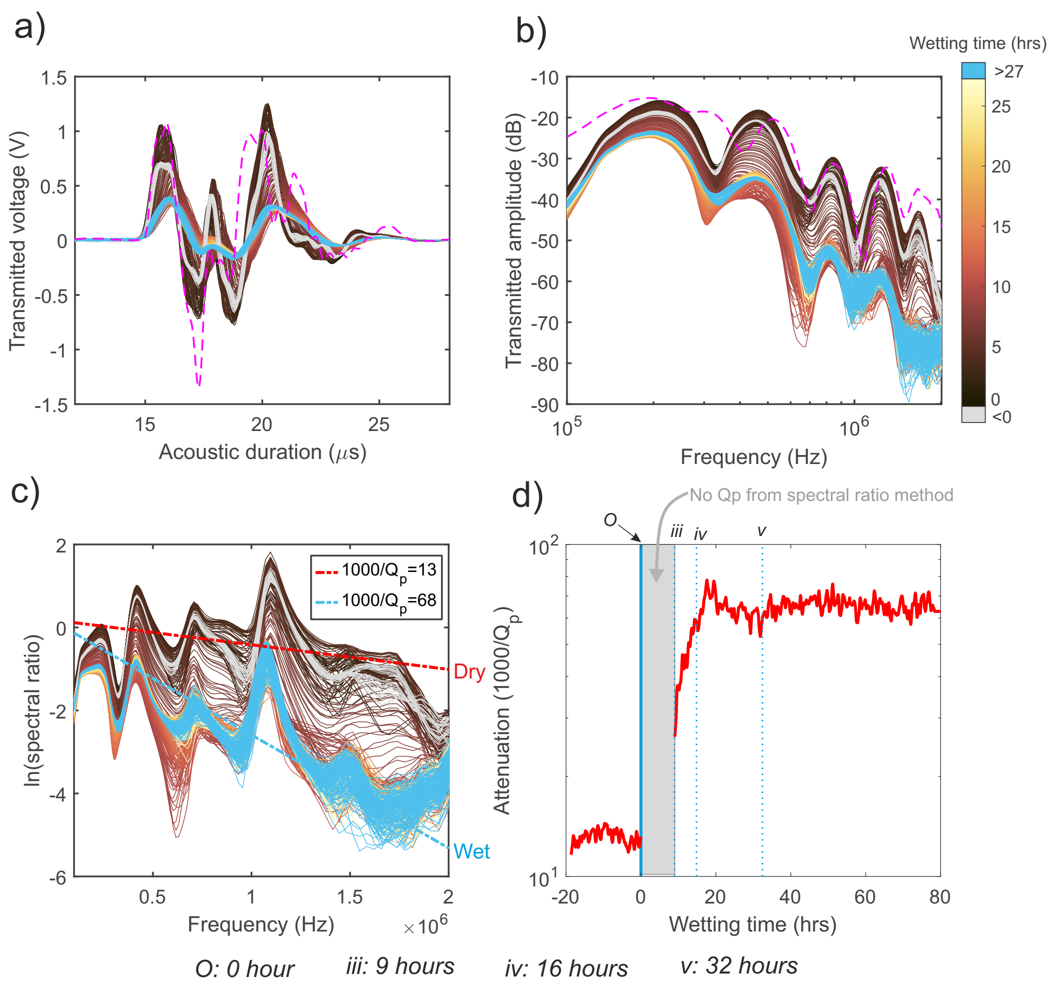

Figure 7. Direct waves in (a) time domain and (b) frequency domain. Grey and light blue denoted the dry and equilibrium wetting stages of Herrnholz granite. Magenta represented data from the aluminum specimen. (c) Natural logarithm of the ratio of Herrnholz granite to aluminum in Fourier amplitudes. The slope was given to show how the P-wave quality factor of the granite specimen, Q_p, evolved from 87 (red dash, dry) to 16 (blue dash, wet). (d) Inverse P-wave quality factor versus wetting time (blue dashed lines indicated some turning points).

well within 18 hour. P-wave data after 27 hours (light blue) remained stable until the end of the measurement. Waveforms from the aluminum specimen (dashed magenta line) were also shown and aligned at the P-wave first arrival for visualization purpose. The natural logarithm of the spectral ratio of transmitted amplitude for the Herrnholz granite to aluminum was given as:

$$\ln\left(\frac{A_1}{A_2}\right) = \left(\frac{1}{Q_1 v_1} - \frac{1}{Q_2 v_2}\right)\pi x f + \ln\left(\frac{G_1}{G_2}\right) \tag{3}$$

and was shown in Figure 7(c). $1/Q_i$ $(i = 1, 2)$ is the inverse quality factor of the direct P-wave phase. $1/Q_i$ could be simply stated as the percentage loss of carried energy in the direct P-wave phase where a high value denotes high attenuation, and vice versa. The term $\left(\frac{1}{Q_1 v_1} - \frac{1}{Q_2 v_2}\right)$ can be found from the slope of the line fitted to $\ln\left(\frac{A_1}{A_2}\right)$ because $\frac{G_1}{G_2}$ is independent of frequency. Q_2 (aluminum) is extremely high (about 1.5 x 10^5 from Zemanek and Rudnick (1961)) compared to that for rocks (tens to hundreds) so that the term $\frac{1}{Q_2 v_2}$ is ignored. Q_1, which represents the Q_p of Herrnholz granite, was derived using the variation in P-wave velocity as the water content increased.

In Figure 7(d), prior to introducing water, $1000/Q_p$ remained stable (12 ± 1). We found the fitting of $1000/Q_p$ failed using the spectral ratio method from time O to iii while the rock experienced progressive wetting. It could be not possibly appropriate to use a constant $1000/Q_p$ to depict complicated changes in the transmitted amplitude at different frequencies during the progressive wetting – $1000/Q_p$ could be frequency-dependent. After time iii, $1000/Q_p$ increased by 37 up to time iv at 16 hours, slowly stabilized until time iv at 32 hours. After time v, less variations was observed in $1000/Q_p$ (68 ± 5).

4.2 Moisture-induced surface deformation

Using the DIC methods, 744 images were analyzed over 98 hours and we observed extensional strains in both the horizontal (x) and vertical (y) directions. The vertical expansion particularly provided an useful insight of the moving wetting front. We here similarly use the contour line ($= \times 10^{-4}$, indicated by the white dashed line) of the vertical strain to track the infiltration front in Figure 8. We presented vertical strain fields from time i to v which were turnings of ultrasonic attributes previously defined in Section 4.1. We found the wetting front reached approximately $y = \sim 9$ mm by time i or 1.3 hours (Figure 8(a)), ~ 11 at time ii or 3.2 hours (Figure 8(b)), ~ 17.5 mm at 7 hours (Figure 8(c)), 20.5

mm at time *iii* or 9 hours (Figure 8(d)), and 28 mm at time *iv* or 16 hours (Figure 8(e)). The vertical strain front (ϵ_{yy}) progressed past the ROI (region of interest) at time v or 32 hours in Figure 8(f); the magnitude of vertical strain was $\sim 10^{-4}$ over the entire ROI at this time. Peaks in the vertical strain field between $10 - 20 \times 10^{-4}$ were observed around the upper edge of ROI and they decreased below 5×10^{-4} at $y = \sim 9$ mm. In Figure 8(a), three dark blue patches can be observed in the top of the ROI, which corresponded to the location of the three aluminum blocks placed on the filter paper. We believed this results in a slightly heterogeneous distribution of the water on the top surface of the contact regions.

When infiltration reached 16 hours, ahead of wetting front, water vapor or a small amount of liquid water intrusion into the local heterogeneity (such as microcracks) caused extension in few small patches ($\sim$ 10 mm $\times$ 5 mm) with strains of $\sim$ 0.8 to $1{\times}10^{-4}$ (see Figure 8(e)). This was also supported by the observation at 32 hours: the wetting front evolved slightly non-uniformly from left to right. The position of the ultrasonic monitoring pair was installed 20 mm below the wetting surface and the correlation between surface strain and ultrasonic changes will be discussed in Section 5.2. Results for the horizontal strain at the same six time intervals were provided in Figure S7 of the Supporting Information to give a tabular summary of the expansion process.

5 Discussion

5.1 Observed ΔV_p in nanopores in response to water infiltration

P-wave velocity changes, ΔV_p, observed in the free-standing progressive wetting test are discussed here. P-wave velocity increase was observed as ΔV_p increased by 520 m/s from time *ii* to *iv*. From the vertical strain evolution shown in Figure 8(b) to (e), the wetting region is almost symmetrical around the transmitter-receiver straight ray path and overlaps with the P-wave first Fresnel zone (P-FFZ). The minor radius size of the P-FFZ, R_1, at the frequency of 600 to 1000 kHz, ranges between 8.7 to 11.3 mm and will be discussed in Section 5.2.1. After time *iv*, the wetting front fully passed P-FFZ (Figure 8(f)), ΔV_p stabilized with less than a 2 % variation over tens of hours. This indicates that a stable equilibrium has been reached between water wetting in the interior of the specimen and evaporation through the specimen's surfaces.

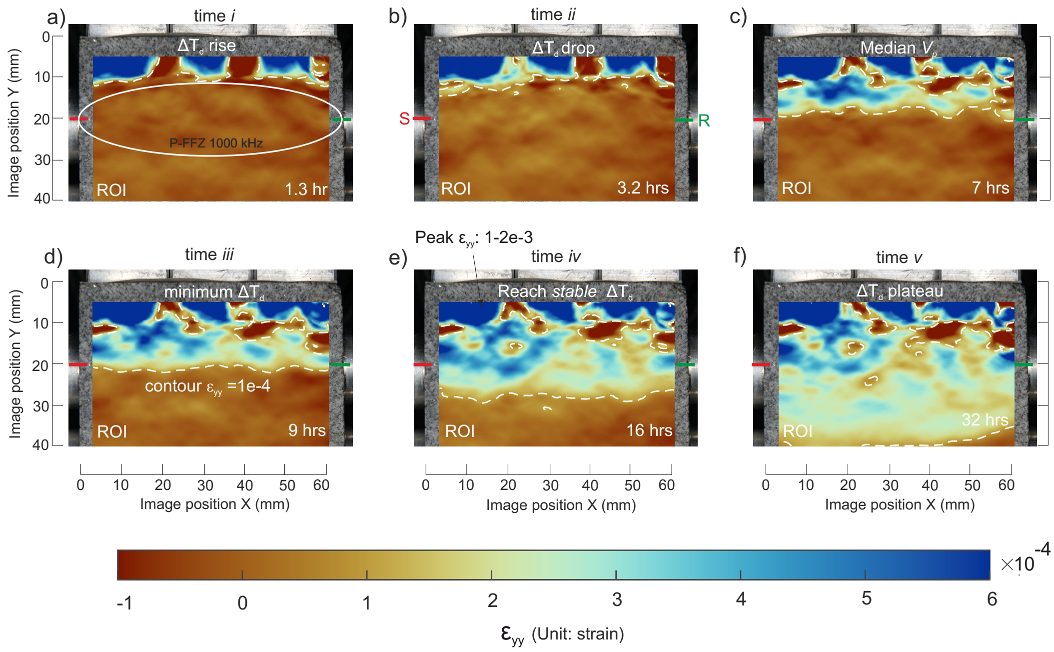

Figure 8. Vertical strain (ϵ_{yy}) evolution on the front surface of the granite specimen (ROI: 58 mm in width and 40 mm in height) as water was applied. Wetting time equal to 0 hour denoted the start of water application to the top surface of the specimen. Times i to v were the times previously defined in the ultrasonic signature analysis.

5.1.1 Squirt flow or Gassmann theory in microcracked nanopore-dominated media?

We modeled P-wave velocity increase in saturated Herrnholz granite within the context of classic theories of fluid substitution in porous media. Gassmann theory was validated at sufficiently low frequency (e.g. *in situ* seismic monitoring below 100 Hz and sonic logging below tens of kHz) at which fluid pressures gradients within interconnected pores, induced by elastic waves, can be dissipated within sufficient time (Gassmann, 1951; Biot, 1956). To extend the Gassmann theory to laboratory ultrasonic frequency (hundreds of kHz to few MHz), the average pore size ($\hat{d}$) must be much smaller than the viscous skin depth $\delta = (\eta/\pi f \rho_{\mathrm{f}})^{1/2}$ (Biot, 1956; Johnson et al., 1987; Gor & Gurevich, 2018). η and ρ_f represent the dynamic fluid viscosity (unit: $Pa \cdot s$) and density of the saturating fluid (distilled water) (units: g/cm^3), respectively, and f is the ultrasonic resonant frequency. Table 1 summarises the essential input parameters (e.g. density, modulus, porosity, frequency) from the thin section analysis (Section 2.1), water-accessible porosity measurement (Section 2.2) and elastic piezosensitivity analysis (Section 2.5). We find that the assumption of Gassmann theory is satisfied (Johnson et al., 1987) because $\hat{d} = 10\ nm \ll \delta = 546\ nm$.

Table 1. Parameters for modeling P-wave velocity increase in Herrnholz granite.

Water	K_f (GPa)	$\rho_f (g/cm^3)$	$\eta (Pa \cdot s)$		
	2.2	1	9.4×10^{-4}		
Dry rock	K_{gr} (GPa)	ρ (g/cm^3)	G_{gr} (GPa)	ϕ_s (%)	
	49.4	2.609	31.1	1.53	
Piezo	K_{drs} (GPa)	G_{drs} (GPa)	ϕ_{c0} (%)	α	f (MHz)
	49.7	29.7	0.072	1.1×10^{-3}	1

Approximated water parameters under 23 $°C$ and 1 standard atmosphere. Parameters in dry rocks and piezosensitivity model from thin section analysis (Section 2.1), water-accessible porosity measurement (Section 2.2), and elastic piezosensitivity analysis (Section 2.5).

In Figure 9, we further examine the applicability of the Gassmann theory to P-wave increase in intact rocks. The P-wave velocity offset between Gassmann prediction (*Gass*, gray) and laboratory measurement (*Sat*, blue) for the saturated granite specimen is greater at low effective stress (280 m/s at 5 MPa) and then decreases approaching 0 m/s, until the maximum effective stress (79 m/s at 160 MPa). By comparing the microstructural differences in nanoporous Vycor glass (Levitz et al., 1991; Gor & Gurevich, 2018) and Herrnholz granite, the effects of natural microcrack characteristics of brittle rocks might contribute to this mismatch.

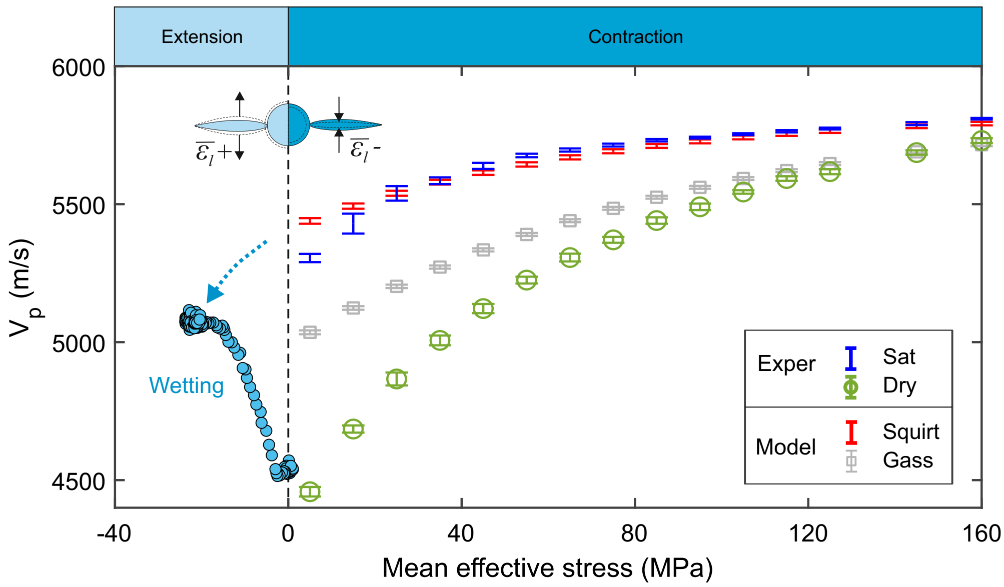

Figure 9. Broadband V_p increase in Herrnholz granite under extensional (left) and contractional (right) stress regimes. Left: V_p evolution from *dry* to *wet* measured in the water imbibition test; Right: V_p measured and modeled in the hydrostatic compression test. *dry* (green, experimentally measured), *Sat* or saturated (blue, experimentally measured), *Gass* or Gassmann theory (gray, model prediction) and *Squirt* or squirt flow theory (red, model prediction).

Mavko and Jizba (1991) quantified the effect of compliant pore spaces or microcracks on elastic stiffening in saturated porous media. This is usually referred to the Mavko−Jizba squirt flow theory. The entire pore space is partitioned into a few subsets of stiff and compliant spaces. Compliant pore spaces are presumed to be thin cracks and grain contacts. At sufficiently high effective stress, most of this soft pore space can be compressed to close, or at least be substantially reduced in volume. The stiffness difference between the measurements and Gassmann theory could then be expected to be the result of the unrelaxed/undissipated pore pressure inside the microcracks that resists deformation imposed by the passage of elastic waves. Gurevich et al. (2010) extended this work to a broader frequency range by considering fluid pressure relaxation in penny-shaped gaps between adjacent grains. They inferred that V_p is exactly consistent with the Gassmann theory at a low-frequency limit and transitions to the Mavko−Jizba squirt flow at a high-frequency limit. We followed their methodology and provided the detailed calculation process of V_p at all frequencies in Section 7 of the Supporting Information. Parameters for the squirt flow model used here are provided in Table 1.

To test the validity of squirt flow model, we compared the predicted V_p from the squirt flow model (*Squirt*, red) at 1 MHz (resonant frequency of the ultrasonic transducers and laboratory measurement (*Sat*, blue) for the saturated granite specimen in Figure 9. In general, the error is less than 0.8 % of measured V_p indicating this model is capturing the observed physics. An anomalous V_p offset of 125 m/s between the *Squirt* and *Sat* at 5 MPa could indicate a contact problem between the granite specimen and adjacent transmitter-receiver pair at a low confining pressure. As the effective stress increases, the error between observed and modelled V_p remains below 40 m/s (0.8 % of measured V_p) and the V_p from squirt flow model correlates well with the V_p changes with confinement for the saturated specimen. While the Gassmann theory works well in nanoporous materials as having stiff pore spaces (e.g. Vycor glass) (Levitz et al., 1991; Gor & Gurevich, 2018), we conclude that P-wave velocity increase in water-saturated microcracked nanopore-dominated media can be better modeled using the squirt flow theory.

5.1.2 ΔV_p in granite under extensional and contractional stress regimes

After testing the validity of the squirt flow theory in the tested granite, we then studied V_p increase under both extensional and contractional stress regimes. Hygroscopic expansion occurs in the water imbibition test (see Section 4.2) as is assumed to be a result of generation of adsorption stress (also known as solvation pressure) through adhesion and capillary condensation by Li et al. (2021). They estimated this adsorption stress by multiplying the mean strain (denoted as $\overline{\epsilon_l}$) by the pore-load modulus M_{pl}: $\sigma_s = M_{pl}\overline{\epsilon_l}$. M_{pl} described a linear relation between the adsorption stress and mean strain and quantified the deformability of porous media in response to changes in pore fluid pressure (Prass et al., 2009; Gor & Gurevich, 2018).

The pore-load modulus M_{pl} was assumed to be independent of the gradually wetting process controlled by hygroscopic expansion and was given as $M_{pl} = \frac{3}{1/K - 1/K_{drs}}$. K is the drained bulk modulus of the granite and was measured independently to be 18.8 GPa at 20 % RH by Li et al. (2021). The bulk modulus of the granite without pore space, $K_{gr} = 49.4$ GPa, was determined in Section 2.5. M_{pl} is estimated to be 91 GPa and thus the solvation pressure is derived as a function of $\overline{\epsilon_l}$. Li et al. (2021) suggested the mean hygroscopic strain can be given as $\overline{\epsilon_l} = (2\epsilon_{xx} + \epsilon_{yy})/3$, where ϵ_{xx} and ϵ_{yy} are average horizontal and vertical strains within a rectangular region symmetrical around the transmitter-receiver pair. The dimension of this region is 58 mm $\times$ 20 mm. More details about this region will be discussed in Section 5.2.1.

To maintain consistency in the contractional condition, mean effective stress $\bar{\sigma}_e$ was adopted instead of solvation pressure (σ_s) by considering $\bar{\sigma}_e = -\sigma_s$ in the case of a free-standing specimen where the specimen was subjected to a zero external stress state. Changes in P-wave velocity and the calculated solvation pressure from the water imbibition test were shown as solid blue circles on the left side in Figure 9. When the specimen saturation changed from ambient humidity conditions (around 20 %) to progressively wetting, V_p and $\Delta\sigma_s$ increased by 520 m/s and 23.9 MPa, respectively. V_p at 0 MPa in the water imbibition test was slightly higher (60 m/s) than V_p at 5 MPa in the hydrostatic compression test. This slight discrepancy was because the ultrasonic monitoring required $\sim$ 5 MPa of confining pressure to generate a proper bond at the contact surface. The steady *Wet* V_p at 23.9 MPa in the water imbibition test could serve as the bound constraint of V_p in the saturated granite at the same $\bar{\sigma}_e$. Following the blue dash arrow in Figure 9, it was possible that the changes seen in V_p between *Wet* and *Sat* V_p could be explained by that squirt flow theory. This may indicate the squirt flow theory could be also valid for extensional stress regimes, but this requires more validation work. For example, in the freestanding wetting test, rock cannot reach the fully saturation status through water imbibition; however, squirt flow theory was developed on the assumption of full saturated rocks. The observed consistency in V_p between *Wet* and *Sat* provides a straightforward understanding of P-wave velocity increase in saturated microcracked nanopore-dominated media spanning stress regimes in both contraction and extension.

5.2 Variations in transmitted amplitude due to water imbibition

Our results indicated that the squirt flow mechanism can account for P-wave velocity increase in nanopore-dominated granite, and could also be one of the major causes of seismic attenuation of passing elastic waves. In this section, changes in the transmitted amplitude of the direct P waves at high frequency were investigated and correlated with simultaneous surface deformations. We found that the transmitted energies at relatively high frequencies were much more sensitive to the approach of a wetting front than at low frequencies (see Figure 6(b)). As a result, we focused attenuation on the high-frequency transmitted amplitude changes for the direct waves ΔT_d (orange solid line) between 600 to 1000 kHz, shown in Figure 10. Imaged strain was averaged within a rectangular box *ROI-1* with dimensions of 60 ×30 mm that was symmetrical along the transmitter-receiver straight ray path. ΔT_d and ΔT_c were correlated with imaged strain evolution (left: horizontal or ϵ_{xx}, right: vertical or or ϵ_{yy}). Times O to v, delineated by the vertical dashed lines, corresponded to the same times given in Section 4.1.

5.2.1 *Direct P wave:* ΔT_d

A peculiar observation was made with ΔT_d after the initial introduction of the water to the specimen. ΔT_d initially remained stable until time i when the wetting front was inside box *ROI-1*. The theoretical R_1 of P-FFZ was 11.3 mm at 600 kHz and 8.7 mm at 1000 kHz, respectively (Equation 1). Comparing the relative position of wetting front and P-FFZ, the ΔT_d plateau remained because the direct P-wave phase mirrored the elastic changes within the P-FFZ. The ΔT_d plateau was followed by a small increase from 0 dB at time i to 10.4 dB at time *ii*. A similar increase was also observed in the P-wave amplitude (first peak) in water imbibition experiments on Sherwood sandstone (mean pore throat diameter of 18 μm, see David, Barnes, et al. (2017)). Since the proposed mechanism is related to squirt flow that only accounted for seismic attenuation, there should exist another mechanism for seismic amplification.

5.2.2 *Analytical solution of plane wave propagation to explain* ΔT_d

We aim to provide an explanation for the increase in ΔT_d starting from elastic wave reflection and refraction between wetting front and incident P waves in P-FFZ. We adopted a similar explanation to that provided by Kovalyshen (2018) where the varying moisture

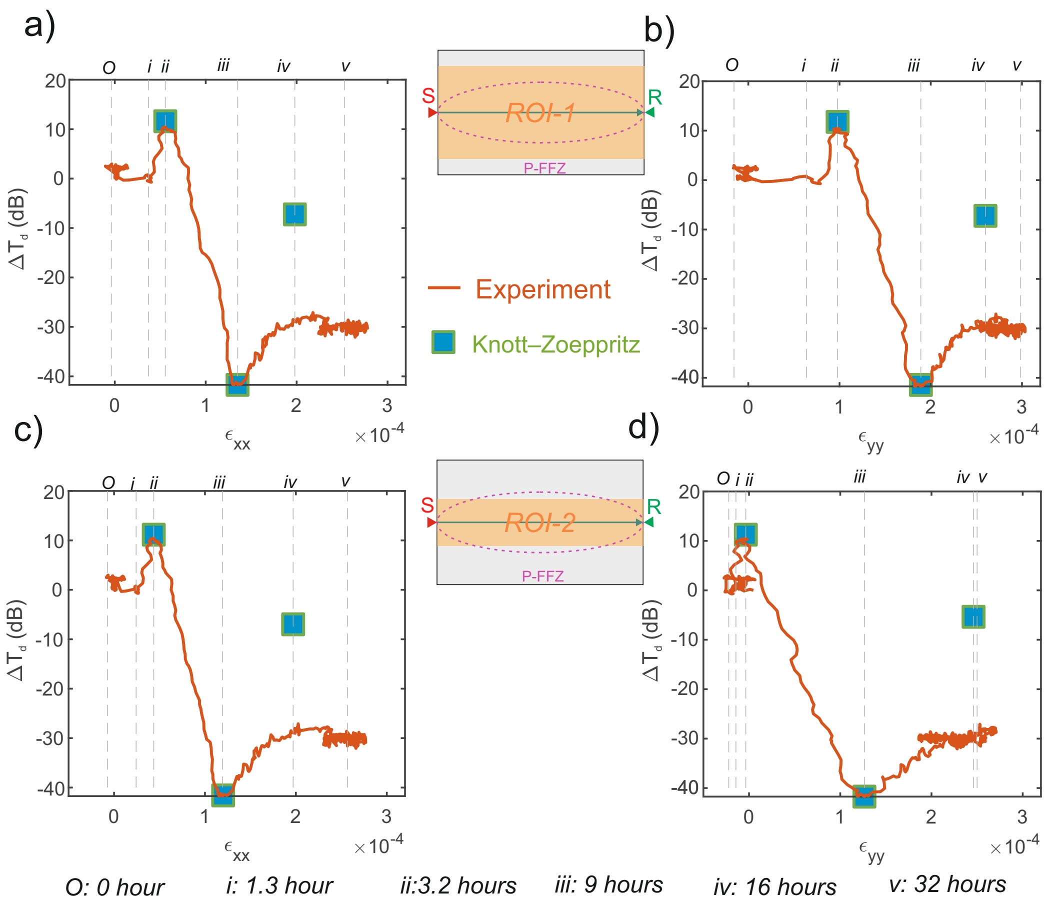

Figure 10. Transmitted amplitude of direct waves from experimental measurement (orange solid line) and theoretical analysis (square symbol) evolution with imaged strain (left: horizontal or ϵ_{xx}, right: vertical or or ϵ_{yy})). Strain was averaged within box *ROI-1* for a) and b), and box *ROI-2* for c) and d), respectively. Vertical grey dashed lines denoted times O to v that were previously defined in ultrasonic signature analysis.

conditions changed the material properties and contributed to the presence of a distinct layer in the medium. We suggested this layer occurred at the wetting front and had properties of both the dry and wet granite across this heterogeneity. This layer was assumed to be ideally flat and sharp and represented the solid-solid interface of the fully saturated (above) and dry (below) regions. The point transmitter and receiver were assumed to generate and receive elastic waves. For the dry phase, $\rho = 2.609\ g/cm^3, V_p = 4550\ m/s$ and $V_s = 2750\ m/s$. For the wetting phase, $\rho = 2.63\ g/cm^3, V_p = 5300\ m/s$ and $V_s = 2850\ m/s$ (measured data from a hydrostatic compression test at a confining pressure of 5 MPa). In Figure 11(a), the wetting front was located above the transmitter-receiver straight ray path. Depending on the incident angle θ, incident P waves could arrive at the receiver directly along the shortest path, i.e., $\theta = 90°$, along the green solid line. At $\theta < 90°$, incident P waves along the green dashed line will reflect on the interface, convert into critically refracted P (denoted as Pp) and S (denoted as Ps) waves and arrive at the receiver with a time delay from the direct P waves. We adopted the same nomenclature as Kovalyshen (2018).

We presented the complete solution (green line) of the incident plane P-wave reflection coefficient R_p on the solid-solid interface, solved using Knott−Zoeppritz equations (Knott, 1899; Zoeppritz, 1919; Mavko et al., 2020, Section 3.5) in Figure 11(c). Unit conversion between R_p (left y-axis) and ΔT_d (right y-axis) was given by $\Delta T_d = 20\log_{10}(1 + R_p)$. A turning point of 60° denoted the grazing angle beyond which total internal reflection occurred with R_p close to 1. When the wetting front arrived to the top co-vertex of 600 kHz P-FFZ at $R_1 \approx 11$ mm or $\theta \approx 71°$, refracted P and S waves started to affect the initial direct P wave and enhanced the amplitude with synthetic waveforms. From time i to ii, the wetting front continuously moved downwards with a vertical distance away from the transmitter-receiver straight ray path from an averaged 11 mm to an averaged 9 mm. This observation matched well with the theoretical R_1 of P-FFZ, which is 11.3 mm for 600 kHz and 8.7 mm for 1000 kHz. The slight difference could be due to the definition of the dry/wet region (strain below and above $1{\times}10^{-4}$), position estimate of the non-uniform wetting front, the gap between experimental and ideal conditions (e.g. finite-dimension specimen, heterogeneity in saturation). Simultaneous monitoring of ultrasonic and DIC imaging effectively constrained the P-FFZ size which has allowed us to develop a model to better describe these observations. We concluded that from time i to ii, the wetting front continuously interacted with the P-FFZ, characterised by the frequency increasing from

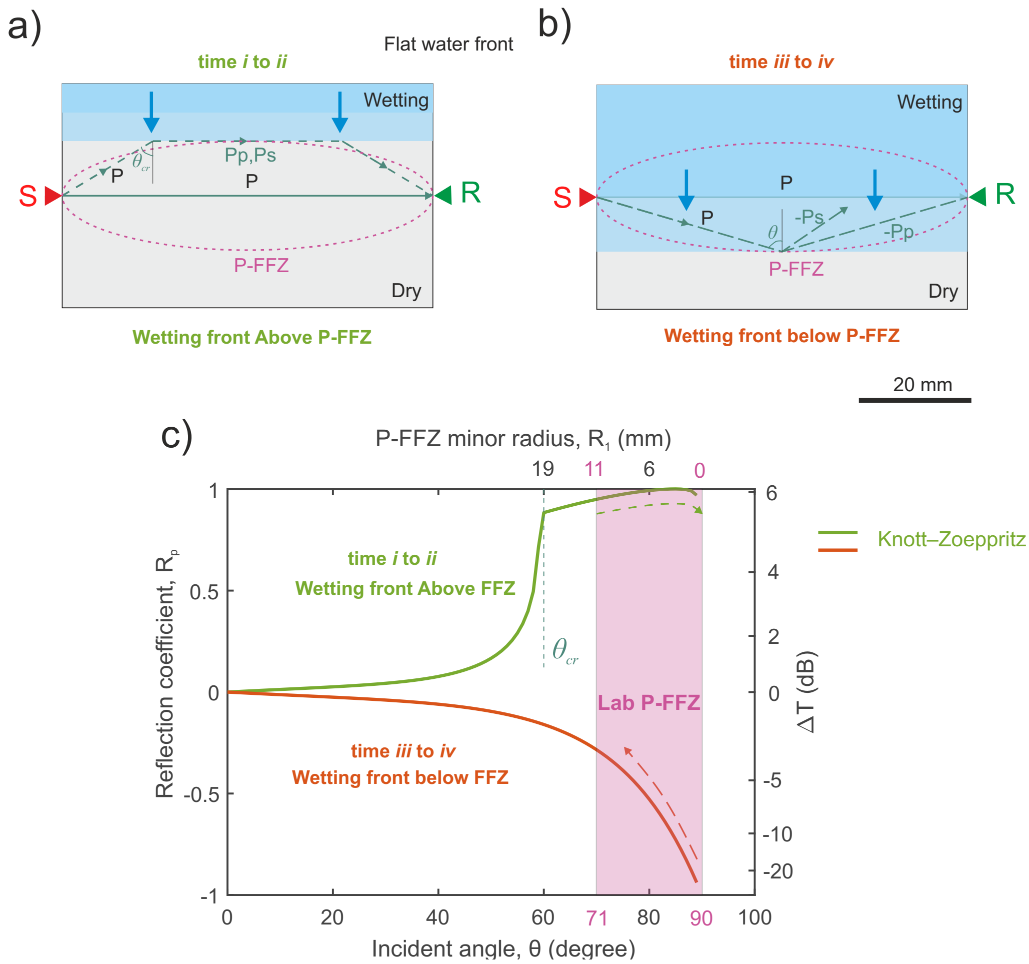

Figure 11. Reflection and refraction of incident P waves on the wetting front. a) Wetting front migrated from the top surface of the specimen to interact with the top co-vertex of the P-FFZ. b) Wetting front moved from the transmitter-receiver straight ray path to the bottom co-vertex of the P-FFZ. c) Reflection coefficient R_p in a) and b) by solving the KnottZoeppritz equation (solid lines). The pink shaded area denoted the minor radius range R_1 of the laboratory P-FFZ.

600 kHz. The experimentally observed ΔT_d was enhanced by 10.4 dB, compared to the theoretical estimate of 11.6 dB shown in Figure 11(c).

Proper correlation of transmitted amplitude changes with surface deformation required an understanding of the physics occurring in the same region. Inconsistent variation between ΔT_d and ϵ_{xx} or ϵ_{yy} from time O to i originated from the size difference between the DIC ROI and P-FFZ. This motivated us to use another rectangular box *ROI-2* (dimension: 60 $\times$16 mm) as the new DIC ROI where the averaged ϵ_{xx} and ϵ_{yy} within *ROI-2* were shown in Figure 10(c) and (d). At time O, i and ii (with a similar finding in time iv and v) there was almost the same strain, which suggested an acceptable overlap between the DIC ROI (box) and F-PPZ (ellipse). From time ii to iii, the wetting front entered all P-FFZs between 600 to 1000 kHz. ΔT_d decreased relatively linearly with the imaged strain until the maximum attenuation of -41.6 dB was reached. At time iii, the wetting front slightly surpassed the position of the transmitter-receiver straight ray path and the amplitude sign of refracted P and S waves will be opposite to the direct P wave with a phase shift of 180° as shown in Figure 11(b). No total internal reflection occurred. The theoretical estimation of ΔT_d was given as -41.8 dB at $\theta \approx 88.5°$, compared to the experimental observation of -41.6 dB.

Once the wetting front passed the transmitter-receiver straight ray path, ΔT_d recovered after time iii. ΔT_d remained at -30 dB with 1 dB variation at time iv when the wetting front leaved the P-FFZ. The orange line in Figure 11(c) was the Knott$-$Zoeppritz solution, and showed R_p that slowly recovered from -48 dB at $\theta \approx 89°$ ($R_1 \approx 0$ mm) to -7.2 dB at $\theta \approx 71°$.

The difference between experimental observations (-30 dB) and the theoretical estimations (-7.2 dB) could originate from hygroscopic expansion and squirt flow. Hygroscopic expansion due to water infiltration occurred and reached a a mean extensional strain of 2.6×10^{-4} within *ROI-2*. This induced an internal solvation pressure of 23.9 MPa. Hygroscopic expansion reduces the effective normal stress (0 to -23.9 MPa, where minus denoted extension) across the contact area of microcracks filled with water. Less ultrasonic wave amplitude was transmitted through the weakly contacted microstructure. When elastic stress waves passed the saturated region, the microcracks were compressed and local pressure gradients were created. We suggested the pore fluid absorbed along the microcracks will squirt into stiff pores against internal friction so that the transmitted energy was partly transformed into heat energy. It has been previously noted that the squirt flow dominates at zero effective stress and almost disappears when microcracks close (Mavko & Jizba, 1991; Gurevich et al., 2010); hygroscopic expansion can be expected to increase pore aperture, and therefore enhance the squirt flow effect, resulting in higher ΔT_d. The combined effects of squirt flow and hygroscopic expansion will decrease the ΔT_d.

Note that it is not sufficient mature to extend the explanation for the changes in ΔT_d modelled by two-layered medium to all other water imbibition experiments. David et al. (2018) checked their ultrasonic dataset tested on 12 different rocks during the water imbibition experiments. They adopted the similar assumptions by Kovalyshen (2018) and calculated the reflection coefficients from Knott−Zoeppritz solution and experimental measurements. They found that although successful in 3 tests, the assumption failed in 9 tests due to the small values of the reflection coefficients from Knott−Zoeppritz solution, and the delay in arrival time of the reflected waves in the tested rocks. We realized that in our study, Knott−Zoeppritz solution was successfully applied to account for changes in ΔT_d; however, for other scenarios, there could be other accompanying underlying mechanisms, i.e. moisture diffusion (David et al., 2018).

6 Conclusions

Realizing the gap in the understanding of elastic variations between macropores and nanopores in microcracked media, we quantified moisture-induced elastic changes in intact Herrnholz granite, a microcracked nanopore-dominated medium, through a laboratory time-lapse acousto-mechanical study. Changes in P-wave velocity and ultrasonic wave amplitude were examined over 98 hours utilizing time-lapse ultrasonic monitoring. Simultaneous digital image correlation was performed to track the wetting front in real-time and calculate the adsorption-induced strain and stress.

While Gor and Gurevich (2018) confirmed the validity and applicability of Gassmann theory into channel-like nanoporous media, we found that there exists a breakdown of Gassmann theory in microcracked nanopore-dominated media. To bridge the gap, we verified that P-wave velocity increase in such media can be properly modeled in the framework of classical squirt flow theory, which has been validated in many microcracked macropore-dominated media. This enables the possibility of applying the mature theory in conventional rock physics to nanopore-dominated media. We also found it could be possible to extend the applicability of squirt flow theory from contractional to extensional stress regimes, which is crucial to capture the response of microcracked media to fluid substitution from deep underground to near-surface condition. However, more validation work is required in the future.

The transmitted amplitude changes in the direct P waves are well-correlated with moisture-induced strain observed around first Fresnel zone. Ultrasonic attributes show amplification, attenuation and recovery in response to the approach of the wetting front. After a comprehensive study of analytical analysis and experimental observation, we conclude that these attributes behave in a predictable manner, which is assumed to be associated with the elastic wave propagation near the first Fresnel zone and reflection/refraction on the wetting front. This finding provides ability of using elastic waves propagation to quantify elastic changes in porous media as a result of gradual wetting.

7 Supporting Information References

Here are all references used in the Supporting Information: Taylor (1997); Li et al. (2021); Washburn (1921); Njiekak et al. (2018); Li et al. (2022); Martiartu and Böhm (2017); Selvadurai et al. (2022); Wu et al. (2021); Akaike (1974); Kurz et al. (2005); Birch (1960); Njiekak et al. (2013); Shapiro (2003); O'Connell and Budiansky (1974); Gurevich et al. (2010); Gassmann (1951); Mavko et al. (2020).

Acknowledgments

The authors would like to thank Elsys company, especially Roman Bertschi, for their hardware and software support for this research. The authors are indebted to Mrs. Sally Selvadurai (scientific Editor at Assist-Ed) for her thorough proofreading and editing of the manuscript. Mr. Wu and Dr. Li are financially supported by the chair, Professor Simon Loew, and the China Scholarship Council. This work was supported by Swiss National Science Foundation (SNSF) R Equip Long-term damage evolution in brittle rocks subject to controlled climatic conditions (Project 170746) and Physical constraints on natural and induced earthquakes using innovative lab-scale experiments: The LabQuake Machine (Project 170766). We thank the support from Dr. Michael Pltze and Markus Rast on measuring pore size distribution and grain density.

We respectfully appreciate the thoughtful and thorough reviews and significant constructive suggestions from Editor Professor Douglas Schmitt and two anonymous reviewers.

Data analyzed in this study are available on the ETH research collection: *https://www.research-collection.ethz.ch/handle/20.500.11850/550969*.

References

Adams, L. H., & Williamson, E. D. (1923, 4). On the compressibility of minerals and rocks at high pressures. *Journal of the Franklin Institute*, *195*(4), 475–529. doi: 10.1016/S0016-0032(23)90314-5

Agersborg, R., Johansen, T. A., Jakobsen, M., Sothcott, J., & Best, A. (2008). Effects of fluids and dual-pore systems on pressure-dependent velocities and attenuations in carbonates. *GEOPHYSICS*, *73*(5), N35-N47. doi: 10.1190/1.2969774

Akaike, H. (1974). A new look at the statistical model identification. *IEEE Transactions on Automatic Control*, *19*(6), 716–723. doi: 10.1109/TAC.1974.1100705

ASTM D-18. (2008). Standard test method for laboratory determination of pulse velocities and ultrasonic elastic constants of rock. In *Annual book of astm standards* (p. 356363). ASTM International.

Aydin, A. (2015). Upgraded ISRM Suggested Method for Determining Sound Velocity by Ultrasonic Pulse Transmission Technique. In R. Ulusay (Ed.), *The isrm suggested methods for rock characterization, testing and monitoring: 2007-2014* (pp. 95–99). Cham: Springer International Publishing. doi: 10.1007/978-3-319-07713-0{_}6

Berryman, J. G. (1980). Longwavelength propagation in composite elastic media II. Ellipsoidal inclusions. *The Journal of the Acoustical Society of America*, *68*(6), 1820–1831. doi: 10.1121/1.385172

Berryman, J. G. (1999). Origin of Gassmanns equations. *GEOPHYSICS*, *64*(5), 1627–1629. doi: 10.1190/1.1444667

Bertschi, R. (2018). *AE-Amp Manual EN* (Tech. Rep.). Mellingerstrasse 12, CH-5443 Niederrohrdorf: https://www.elsys-instruments.com/en/products/ae-amp-preamplifier.php.

Biot, M. A. (1956). Theory of propagation of elastic waves in a fluid saturated porous solid. I. Low frequency range and II. Higher-frequency range. *The Journal of the Acoustical Society of America*, *28*(2), 168–191. doi: 10.1121/1.1908241

Birch, F. (1960). The velocity of compressional waves in rocks to 10 kilobars: 1. *Journal of Geophysical Research (1896-1977)*, *65*(4), 1083–1102. doi: https://doi.org/10.1029/JZ065i004p01083

Blaber, J., Adair, B., & Antoniou, A. (2015). Ncorr: Open-Source 2D Digital Image Correlation Matlab Software. *Experimental Mechanics*, *55*(6), 1105–1122. doi: 10.1007/s11340-015-0009-1

Brace, W. F. (1965). Some new measurements of linear compressibility of rocks. *Journal of Geophysical Research (1896-1977)*, *70*(2), 391–398. doi: https://doi.org/10.1029/JZ070i002p00391

Bracewell, R. N. (1986). *The Fourier Transform and its Applications* (Vol. 31999). McGraw-Hill New York.

Burjánek, J., Gischig, V., Moore, J. R., & Fäh, D. (2017). Ambient vibration characterization and monitoring of a rock slope close to collapse. *Geophysical Journal International*, *212*(1), 297–310. doi: 10.1093/gji/ggx424

Cheng, C. H., & Toksöz, M. N. (1979). Inversion of seismic velocities for the pore aspect ratio spectrum of a rock. *Journal of Geophysical Research: Solid Earth*, *84*(B13), 7533–7543. doi: https://doi.org/10.1029/JB084iB13p07533

Christeson, G. L., Gulick, S. P., Morgan, J. V., Gebhardt, C., Kring, D. A., Le Ber, E., ... Yamaguchi, K. E. (2018, 8). Extraordinary rocks from the peak ring of the Chicxulub impact crater: P-wave velocity, density, and porosity measurements from IODP/ICDP Expedition 364. *Earth and Planetary Science Letters*, *495*, 1–11. doi: 10.1016/J.EPSL.2018.05.013

Coyner, K. B. (1984). *Effects of stress, pore pressure, and pore fluids on bulk strain, velocity, and permeability in rocks* (Unpublished doctoral dissertation). Massachusetts Institute of Technology.

David, C., Barnes, C., Desrues, M., Pimienta, L., Sarout, J., & Dautriat, J. (2017). Ultrasonic monitoring of spontaneous imbibition experiments: Acoustic signature of fluid migration. *Journal of Geophysical Research: Solid Earth*, *122*(7), 4931–4947. doi: https://doi.org/10.1002/2016JB013804

David, C., Barnes, C., Sarout, J., Dautriat, J., & Pimienta, L. (2018). Reply to Comment by Y. Kovalyshen on Ultrasonic monitoring of spontaneous imbibition experiments: precursory moisture diffusion effects ahead of water front. *Journal of Geophysical Research: Solid Earth*, *123*(8), 6610–6615. doi: doi:10.1029/2018JB016133

David, C., Sarout, J., Dautriat, J., Pimienta, L., Michée, M., Desrues, M., & Barnes, C. (2017). Ultrasonic monitoring of spontaneous imbibition experiments: Precursory moisture diffusion effects ahead of water front. *Journal of Geophysical Research: Solid*

Earth, *122*(7), 4948–4962. doi: doi:10.1002/2017JB014193

Diederichs, M. S. (2007). Mechanistic interpretation and practical application of damage and spalling prediction criteria for deep tunnelling. *Canadian Geotechnical Journal*, *44*(9), 1082–1116.

Dobrzanski, C. D., Gurevich, B., & Gor, G. Y. (2021). Elastic properties of confined fluids from molecular modeling to ultrasonic experiments on porous solids. *Applied Physics Reviews*, *8*(2), 21317. doi: 10.1063/5.0024114

Eitzen, D. G., & Wadley, H. N. G. (1984). Acoustic emission: establishing the fundamentals. *Journal of research of the National Bureau of Standards*, *89*(1), 75–100.

Gassmann, F. (1951). Elastic waves through a packing of spheres. *GEOPHYSICS*, *16*(4), 673–685. doi: 10.1190/1.1437718

Glaser, S. D., Weiss, G. G., & Johnson, L. R. (1998, 9). Body waves recorded inside an elastic half-space by an embedded, wideband velocity sensor. *The Journal of the Acoustical Society of America*, *104*(3), 1404–1412.

Gor, G. Y., & Bernstein, N. (2016). Revisiting Bangham's law of adsorption-induced deformation: changes of surface energy and surface stress. *Physical Chemistry Chemical Physics*, *18*(14), 9788–9798.

Gor, G. Y., & Gurevich, B. (2018). Gassmann theory applies to nanoporous media. *Geophysical Research Letters*, *45*(1), 146–155. doi: https://doi.org/10.1002/2017GL075321

Gor, G. Y., & Neimark, A. V. (2010). Adsorption-induced deformation of mesoporous solids. *Langmuir*, *26*(16), 13021–13027. doi: 10.1021/la1019247

Gurevich, B., Makarynska, D., de Paula, O. B., & Pervukhina, M. (2010). A simple model for squirt-flow dispersion and attenuation in fluid-saturated granular rocks. *GEOPHYSICS*, *75*(6), N109-N120. doi: 10.1190/1.3509782

Han, D.-H. (1987). *Effects of porosity and clay content on acoustic properties of sandstones and unconsolidated sediments* (Unpublished doctoral dissertation). Stanford University.

Hill, R. (1952, 5). The Elastic Behaviour of a Crystalline Aggregate. *Proceedings of the Physical Society. Section A*, *65*(5), 349–354. doi: 10.1088/0370-1298/65/5/307

Johnson, D. L., Koplik, J., & Dashen, R. (1987). Theory of dynamic permeability and tortuosity in fluid-saturated porous media. *Journal of Fluid Mechanics*, *176*(-1), 379. doi: 10.1017/S0022112087000727

Johnston, D. H., Toksöz, M. N., & Timur, A. (1979). Attenuation of seismic waves in dry and saturated rocks: II. Mechanisms. *GEOPHYSICS*, *44*(4), 691–711. doi: 10.1190/1.1440970

King, M. S. (1966). Wave velocities in rocks as a function of changes in overburden pressure and pore fluid saturants. *GEOPHYSICS*, *31*(1), 50–73. doi: 10.1190/1.1439763

Knight, R., & Nolen-Hoeksema, R. (1990). A laboratory study of the dependence of elastic wave velocities on pore scale fluid distribution. *Geophysical Research Letters*, *17*(10), 1529–1532. doi: https://doi.org/10.1029/GL017i010p01529

Knott, C. G. (1899). Reflexion and refraction of elastic waves, with seismological applications. *The London, Edinburgh, and Dublin Philosophical Magazine and Journal of Science*, *48*(290), 64–97.

Kovalyshen, Y. (2018). Comment on Ultrasonic monitoring of spontaneous imbibition experiments: precursory moisture diffusion effects ahead of water front by David et al. (2017). *Journal of Geophysical Research: Solid Earth*, *123*(8), 6607–6609. doi: doi:10.1029/2018JB016040

Kurz, J. H., Grosse, C. U., & Reinhardt, H. W. (2005, 6). Strategies for reliable automatic onset time picking of acoustic emissions and of ultrasound signals in concrete. *Ultrasonics*, *43*(7), 538–546. doi: 10.1016/J.ULTRAS.2004.12.005

Kuster, G. T., & Toksöz, M. N. (1974). Velocity and attenuation of seismic waves in two-phase media: Part I, Theoretical formulations. *GEOPHYSICS*, *39*(5), 587–606. doi: 10.1190/1.1440450

Landrø, M. (2001). Discrimination between pressure and fluid saturation changes from timelapse seismic data. *GEOPHYSICS*, *66*(3), 836–844. doi: 10.1190/1.1444973

Le Breton, M., Bontemps, N., Guillemot, A., Baillet, L., & Larose, . (2021, 5). Landslide monitoring using seismic ambient noise correlation: challenges and applications. *Earth-Science Reviews*, *216*, 103518. doi: 10.1016/J.EARSCIREV.2021.103518

Levitz, P., Ehret, G., Sinha, S. K., & Drake, J. M. (1991). Porous vycor glass: The microstructure as probed by electron microscopy, direct energy transfer, smallangle scattering, and molecular adsorption. *The Journal of Chemical Physics*, *95*(8), 6151–6161. doi: 10.1063/1.461583

Li, Y., Leith, K., Perras, M. A., & Loew, S. (2021). Digital image correlationbased analysis of hygroscopic expansion in Herrnholz granite. *International Journal of Rock Mechanics and Mining Sciences*, *146*, 104859. doi: 10.1016/J.IJRMMS.2021.104859

Li, Y., Leith, K., Perras, M. A., & Loew, S. (2022). Effect of Ambient Humidity on the Elasticity and Deformation of Unweathered Granite (submitted). *Journal of Geophysical Research: Solid Earth*.

Loew, S., Gschwind, S., Gischig, V., Keller-Signer, A., & Valenti, G. (2017). Monitoring and early warning of the 2012 Preonzo catastrophic rockslope failure. *Landslides*, *14* (1), 141–154.

Martiartu, N. K., & Böhm, C. (2017). *TTomo: Straight ray tomography.* Seismology and Wave Physics group at ETH Zurich. Retrieved from `https://cos.ethz.ch/software/research/ttomo.html`

Mavko, G., & Jizba, D. (1991). Estimating grainscale fluid effects on velocity dispersion in rocks. *GEOPHYSICS*, *56* (12), 1940–1949. doi: 10.1190/1.1443005

Mavko, G., Mukerji, T., & Dvorkin, J. (2020). *The Rock Physics Handbook*. Cambridge, United Kingdom: Cambridge University Press. doi: 10.1017/9781108333016

Mavko, G., & Nur, A. (1979). Wave attenuation in partially saturated rocks. *GEOPHYSICS*, *44* (2), 161–178. doi: 10.1190/1.1440958

McBain, J. W., & Ferguson, J. (1927). On the nature of the influence of humidity changes upon the composition of building materials. *The Journal of Physical Chemistry*, *31* (4), 564–590.

Müller, T. M., Gurevich, B., & Lebedev, M. (2010). Seismic wave attenuation and dispersion resulting from wave-induced flow in porous rocks - A review. *GEOPHYSICS*, *75* (5). doi: 10.1190/1.3463417

Murphy III, W. F. (1982). *Effects of microstructure and pore fluids on the acoustic properties of granular sedimentary materials* (Unpublished doctoral dissertation). Stanford University.

Njiekak, G., Schmitt, D. R., & Kofman, R. S. (2018, 12). Pore systems in carbonate formations, Weyburn field, Saskatchewan, Canada: Micro-tomography, helium porosimetry and mercury intrusion porosimetry characterization. *Journal of Petroleum Science and Engineering*, *171*, 1496–1513. doi: 10.1016/J.PETROL.2018.08.029

Njiekak, G., Schmitt, D. R., Yam, H., & Kofman, R. S. (2013, 6). CO2 rock physics as part of the Weyburn-Midale geological storage project. *International Journal of Greenhouse Gas Control*, *16*, S118-S133. doi: 10.1016/j.ijggc.2013.02.007

Norris, A. N. (1985, 3). A differential scheme for the effective moduli of composites. *Mechanics of Materials*, *4* (1), 1–16. doi: 10.1016/0167-6636(85)90002-X

Nur, A., & Simmons, G. (1969). The effect of saturation on velocity in low porosity rocks.

Earth and Planetary Science Letters, *7*(2), 183–193. doi: 10.1016/0012-821X(69)90035-1

O'Connell, R. J., & Budiansky, B. (1974). Seismic velocities in dry and saturated cracked solids. *Journal of Geophysical Research (1896-1977)*, *79*(35), 5412–5426. doi: https://doi.org/10.1029/JB079i035p05412

O'Connell, R. J., & Budiansky, B. (1977). Viscoelastic properties of fluid-saturated cracked solids. *Journal of Geophysical Research*, *82*(36), 5719–5735. doi: https://doi.org/10.1029/JB082i036p05719

Page, J. H., Liu, J., Abeles, B., Herbolzheimer, E., Deckman, H. W., & Weitz, D. A. (1995, 9). Adsorption and desorption of a wetting fluid in Vycor studied by acoustic and optical techniques. *Physical Review E*, *52*(3), 2763–2777. doi: 10.1103/PhysRevE.52.2763

Pimienta, L., David, C., Sarout, J., Perrot, X., Dautriat, J., & Barnes, C. (2019). Evolution in seismic properties during low and intermediate water saturation: competing mechanisms during water imbibition? *Geophysical Research Letters*, *46*(9), 4581–4590. doi: 10.1029/2019GL082419

Prass, J., Müter, D., Fratzl, P., & Paris, O. (2009). Capillarity-driven deformation of ordered nanoporous silica. *Applied Physics Letters*, *95*(8), 83121. doi: 10.1063/1.3213564

Pyrak-Nolte, L. J., Myer, L. R., & Cook, N. G. (1990). Transmission of seismic waves across single natural fractures. *Journal of Geophysical Research*, *95*(B6), 8617–8638. doi: 10.1029/JB095iB06p08617

Reuss, A. (1929). Computation of the yield point of mixed crystals due to hiring for single crystals. *Math. Phys*, *9*, 49–58.

Saenger, E. H., Lebedev, M., Uribe, D., Osorno, M., Vialle, S., Duda, M., … Steeb, H. (2016). Analysis of high-resolution X-ray computed tomography images of Bentheim sandstone under elevated confining pressures. *Geophysical Prospecting*, *64*(4), 848–859. doi: https://doi.org/10.1111/1365-2478.12400

Saito, T. (1981). Variation of Physical Properties of Igneous Rocks In Weathering. In *Proceedings of the international symposium on weak rock* (p. 191196). Tokyo.

Schappert, K., & Pelster, R. (2013). Elastic properties of liquid and solid argon in nanopores. *Journal of Physics: Condensed Matter*, *25*(41), 415302. doi: 10.1088/0953-8984/25/41/415302

Schmitt, D. R., Welz, M., & Rokosh, C. D. (2005). High-resolution seismic imaging over thick permafrost at the 2002 Mallik drill site. *BULLETIN-GEOLOGICAL SURVEY OF CANADA*, *585*, 125.

Selvadurai, Letendre, A., & Hekimi, B. (2011). Axial flow hydraulic pulse testing of an argillaceous limestone. *Environmental Earth Sciences*, *64*(8), 2047–2058. doi: 10.1007/s12665-011-1027-7

Selvadurai, P. A., Wu, R., Bianchi, P., Niu, Z., Michail, S., Madonna, C., & Wiemer, S. (2022). A Methodology for Reconstructing Source Properties of a Conical Piezoelectric Actuator Using Array-Based Methods. *Journal of Nondestructive Evaluation*, *41*(1), 23. doi: 10.1007/s10921-022-00853-6

Shapiro, S. A. (2003). Elastic piezosensitivity of porous and fractured rocks. *GEOPHYSICS*, *68*(2), 482–486. doi: 10.1190/1.1567215

Spetzler, J., & Snieder, R. (2004). The Fresnel volume and transmitted waves. *GEOPHYSICS*, *69*(3), 653–663. doi: 10.1190/1.1759451

Taylor, J. (1997). *Introduction to error analysis, the study of uncertainties in physical measurements.*

Thery, R., Guillemot, A., Abraham, O., & Larose, E. (2020). Tracking fluids in multiple scattering and highly porous materials: Toward applications in non-destructive testing and seismic monitoring. *Ultrasonics*, *102*, 106019. doi: https://doi.org/10.1016/j.ultras.2019.106019

Thommes, M., Kaneko, K., Neimark, A. V., Olivier, J. P., Rodriguez-Reinoso, F., Rouquerol, J., & Sing, K. S. W. (2015). Physisorption of gases, with special reference to the evaluation of surface area and pore size distribution (IUPAC Technical Report). *Pure and Applied Chemistry*, *87*(9-10), 1051–1069. doi: 10.1515/pac-2014-1117

Tiennot, M., & Fortin, J. (2020). Moisture-induced elastic weakening and wave propagation in a clay-bearing sandstone. *Géotechnique Letters*, *10*(3), 424–428. doi: 10.1680/jgele.19.00052

Toksöz, M. N., Johnston, D. H., & Timur, A. (1979). Attenuation of seismic waves in dry and saturated rocks: I. Laboratory measurements. *GEOPHYSICS*, *44*(4), 681–690. doi: 10.1190/1.1440969

Voigt, W. (1910). *Lehrbuch der kristallphysik:(mit ausschluss der kristalloptik)* (Vol. 34). BG Teubner.

Walsh, J. B. (1965). The effect of cracks on the compressibility of rock. *Journal of Geophysical Research (1896-1977)*, *70*(2), 381–389. doi: https://doi.org/10.1029/

JZ070i002p00381

Walsh, J. B. (1995). Seismic attenuation in partially saturated rock. *Journal of Geophysical Research: Solid Earth*, *100*(B8), 15407–15424. doi: https://doi.org/10.1029/94JB03264

Wang, L., Rybacki, E., Bonnelye, A., Bohnhoff, M., & Dresen, G. (2021). Experimental investigation on static and dynamic bulk moduli of dry and fluid-saturated porous sandstones. *Rock Mechanics and Rock Engineering*, *54*(1), 129–148. doi: 10.1007/s00603-020-02248-3

Washburn, E. W. (1921, 3). The Dynamics of Capillary Flow. *Phys. Rev.*, *17*(3), 273–283. doi: 10.1103/PhysRev.17.273

Wepfer, W. W., & Christensen, N. I. (1991, 9). A seismic velocity-confining pressure relation, with applications. *International Journal of Rock Mechanics and Mining Sciences & Geomechanics Abstracts*, *28*(5), 451–456. doi: 10.1016/0148-9062(91)90083-X

Winkler, K., & Nur, A. (1979). Pore fluids and seismic attenuation in rocks. *Geophysical Research Letters*, *6*(1), 1–4. doi: 10.1029/GL006i001p00001

Winkler, K., & Nur, A. (1982). Seismic attenuation: Effects of pore fluids and frictionalsliding. *GEOPHYSICS*, *47*(1), 1–15. doi: 10.1190/1.1441276

Wu, R., Selvadurai, P. A., Chen, C., & Moradian, O. (2021). Revisiting piezoelectric sensor calibration methods using elastodynamic body waves. *Journal of Nondestructive Evaluation*, *40*(3), 68. doi: 10.1007/s10921-021-00799-1

Wulff, A., & Mjaaland, S. (2002). Seismic monitoring of fluid fronts: An experimental study. *GEOPHYSICS*, *67*(1), 221–229. doi: 10.1190/1.1451622

Yurikov, A., Lebedev, M., Gor, G. Y., & Gurevich, B. (2018). Sorption-induced deformation and eastic weakening of Bentheim sandstone. *Journal of Geophysical Research: Solid Earth*, *123*(10), 8589–8601. doi: 10.1029/2018JB016003

Zemanek, J., & Rudnick, I. (1961). Attenuation and dispersion of elastic waves in a cylindrical bar. *The Journal of the Acoustical Society of America*, *33*(10), 1283–1288. doi: 10.1121/1.1908417

Zoeppritz, K. (1919). On the reflection and propagation of seismic waves. *Gottinger Nachrichten*, *1*(5), 66–84.